DISSERTATIONES PHYSICAE UNIVERSITATIS TARTUENSIS
66

DISSERTATIONES PHYSICAE UNIVERSITATIS TARTUENSIS
66

JÜRI RAUD

Study of negative glow and positive column regions of capillary HF discharge

TARTU UNIVERSITY
PRESS

This study was carried out at the Institute of Physics, University of Tartu.

The Dissertation was admitted on September 18, 2009, in partial fulfilment of the requirements for the degree of Doctor of Philosophy in physics (optics and spectroscopy) and allowed for defence by the Council of the Institute of Physics, University of Tartu.

Supervisor: Assoc. Prof. Matti Laan, Institute of Physics, University of Tartu, Estonia

Opponents: D.Sc. Boris Krylov, S. I. Vavilov State Optics Institute, Russia

Prof. Emer. Ülo Ugaste, Faculty of Mathematics and Natural Sciences, Tallinn University, Estonia

Defence: October 30, 2009 at the University of Tartu, Estonia

ISSN 1406–0647
ISBN 978–9949–19–228–1 (trükis)
ISBN 978–9949–19–229–8 (PDF)

Tartu Ülikooli Kirjastus
www.tyk.ee
Tellimus nr. 376

CONTENTS

LIST OF ORIGINAL PUBLICATIONS

CC-level publications related to plasma physics

1. Raud, J.; Laan, M.; Aints, M. (2006). The influence of N_2 as trace gas to HF capillary discharge in He. *Journal of Physics D: Applied Physics*, **39**, 2724–2731.
2. Raud, J.; Laan, M. (2009). Positive column of HF discharge in He / N_2 mixture: excitation and ionization mechanisms. *Journal of Physics D: Applied Physics*, **42**, 015205.
3. Denks, V.; Aints, M.; Avarmaa, T.; Choi, J.-S.; Feldbach, E.; Jaaniso, R.; Kasikov, A.; Kirm, M.; Kodu, M.; Lee, M.-S.; Maaroos, A.; Matulevich, Y.T.; Mändar, H.; Raud, J. (2007). Investigation of possible replacement of protective magnesium oxide layer in plasma display panels by barium ternary oxides. *Journal of Physics D: Applied Physics*, **40**, 4503–4507.
4. Matulevich, Y.; Lee, M.; Kim, J.; Choi, J.; Kim, S.; Suh, S.; Zang, D.; Aarik, J.; Aidla, A.; Aints, M.; Raud, J.; Kirm, M. (2006). Ion induced electron emission from different crystalline phase of ZrO_2. *Applied Physics Letters*, **88**, 211504

Other CC-level publications

5. Aitasalo, T.; Hölsä, J.; Kirm, M.; Laamanen, T.; Lastusaari, M.; Niittykoski, J.; Raud, J.; Valtonen, R. (2007). Persistent luminescence and synchrotron radiation study of the $Ca_2MgSi_2O_7:Eu^{2+}$, R^{3+} materials. *Radiation Measurements*, **42**, 644–647.

Conference papers

6. Laan, M.; Raud, J. (2002). HF Capillary discharge: Distribution of radiation along electrodes. *Hakone VIII : International Symposium on High Pressure Low Temperature Plasma Chemistry* (Tartu, Estonia) *Contrib. Papers* 286–290.
7. Raud, J.; Laan, M. (2007). Production of N_2^+ in positive column of HF discharge in He / N_2 mixture. *In: Proceedings: XXVIII international conference on phenomena in ionized gases* (Prague, Czech Republic).
8. Hölsä, J.; Niittykoski, J.; Kirm, M.; Laamanen, T.; Lastusaari, M.; Novak, P.; Raud, J. (2008). Synchrotron Radiation Study of the $M_2MgSi_2O_7:Eu^{2+}$ Persistent Luminescence Materials. *In: Persistent Phosphors 3: 211th ECS Meeting;* (Chicago, Illinois, USA) 1–10.

Author's contribution

Papers 1, 2, 7: Performed most of experimental work and data analysis. Actively participated in preparation of the manuscript.

Papers 3, 4, 6: Participated in setting up the experiment, measurements and data analysis.

Papers 5, 8: Participated in measurements.

1. INTRODUCTION

High excitation/ionization energies and low chemical reactivity of noble gases are the reasons why their discharges have numerous applications: they are used to produce UV and VUV light [Hill, 1993], they are used as an important component in the mixtures of different gas discharge lasers like He:N_2 laser [Jitsuno, 1981], they are used in plasma display panels [Boeuf, 2003] etc. Because of unique properties of helium like high thermal conductivity and the highest excitation energies of its metastable states, discharges in He have been studied during more than 100 years. However, there are still a number of open problems concerning excitation/deexcitation mechanisms of atomic He, formation and recombination of He molecular ions, the energy transfer between He and track gases etc.

The present thesis is focussed on the study of excitation mechanisms of He and ionization mechanisms of N_2 in He / N_2 mixtures in the case of stationary discharge.

It is accepted that the excitation of He atoms could occur mainly via (i) electron impact with ground state He atoms, (ii) electron impact with metastable state He atoms, and (iii) He_2^+ dissociative recombination. However, there is no common viewpoint about the relative importance of He excitation via the latter excitation mechanism. Moreover, for simplification of the interpretation of experimental results, most of studies related to He_2^+ recombination are carried out in afterglow regime as in this case mechanisms (i) and (ii) do not play any role. At the same time the distribution of He_2^+ vibrational states, which determines the efficiency of recombination, in stationary regime differs considerably from that in afterglow regime. Thus, results of afterglow studies are not automatically applicable for stationary discharges.

At low fractions of N_2 (concentration typically < 1%) in the middle pressure He / N_2 mixture discharges the ionization of N_2 occurs either via reaction between He metastable state atom and N_2 (Penning reaction) or via reaction between He_2^+ and N_2 (charge transfer reaction). Because of very high rate constants of these reactions, even small N_2 concentration decreases both the population of He metastable atoms and the concentration He_2^+ thus affecting excitation and ionization schema of He. Different authors estimate the contribution of Penning and charge transfer reactions differently.

The task of the present work is to find out what are the dominating excitation mechanisms of He and ionization mechanisms of N_2 in the negative glow and positive column regions of HF γ -mode discharge.

The study is mostly experimental. The outline of the work is as follows:

An overview of the literature devoted to the present subject is given in chapter 2. At the end of the chapter the research program is introduced.

The experimental set-up (vacuum system, systems of electrical and optical measurements) and the procedures used are described in chapter 3.

Experimental results and discussion are presented in chapter 4. At the beginning of the chapter results of electrical measurements are presented. Using proposed electrical equivalent circuit, plasma current and voltage on the plasma are calculated and electron concentration is determined. On the basis of optical and spectroscopic measurements discharge mode, gas temperature and concentration of He metastable state atoms are determined. The analyses allows to identify He excitation and N_2 ionization mechanisms. At the end of the chapter open problems are pointed out.

The main results of the work are presented in the summaries in English and Estonian.

2. LITERATURE REVIEW

First subsection of the chapter describes HF discharge modes and the characteristic spatial regions of discharge. Following subsections summarizes results of earlier studies concerning excitation and ionization mechanisms in He and He/N_2. At the end of the chapter open problems and research program are presented.

2.1. HF discharge modes

Subsection 2.1 is written on the base of [Raizer, 1991] and [Raizer, 1996].

In a HF discharge electrons oscillate in accordance with external field while ions, as much heavier particles may consider immovable. When electrons vanish from near electrode region, a layer of ions appears (in the literature the layer is called as Near Electrode Space Charge Sheath - NESCS). Depending on the role of NESCS in the gas ionization, two different forms of HF discharge may be distinguished: low (α-mode) and high (γ-mode) current discharge. In the case of α-mode NESCS is broad and weakly conducting, the discharge is mainly sustained by volume ionization. Compared with α-mode, in the γ-mode NESCS is narrower, the ionic current to the electrode is higher, and secondary electron emission from the electrode plays an important role. The transition from α - to γ-mode is a result of breakdown of NESCS. The transition realizes when voltage across NESCS reaches the value equal to the Paschen breakdown threshold.

According to experimental results discharge in both α -and γ-mode can exist at the product of pressure p and discharge length L, $p \cdot L$, which are smaller than a certain critical value $(p \cdot L)_{CR}$. If $p \cdot L > (p \cdot L)_{CR}$ then only γ-mode discharge is possible to ignite. As a rule $(p \cdot L)_{CR}$ is for molecular gases lower than that for atomic gases. Beside p, L the discharge mode depends also on frequency f and current i. At certain fixed values of p, L, f both modes are achievable by varying i, figure 1.

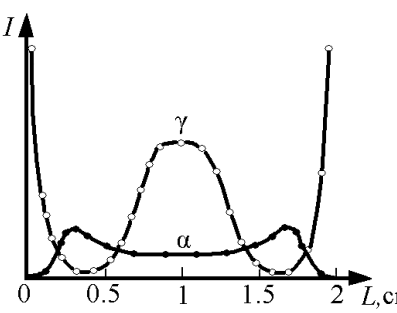

Figure 1. Intensity distribution in the gap of α- and γ-mode discharges. Air, p = 10 Torr, f=13.56 MHz, parallel plate electrode configuration.

At low currents, in the case of α -mode, discharge is concentrated at the middle of the gap detaching away from non-conducting NESCS.

At sufficiently high current the α -mode is transformed into the γ -mode and it leads to the redistribution of the light. In the γ -mode discharge following characteristic spatial regions are presented: NESCS, negative glow (in figure 1 bright regions near electrodes), Faraday dark space (low intensity regions following to the negative glow) and positive column (bright region at the middle of the gap). Next a short overview about the γ -mode discharge regions is given.

(i) NESCS

In α -mode transition to γ -mode, the initial thick ionic layer contracts to the value that is optimal for the self-sustainment. Remaining part of the former layer is converted into electrically neutral plasma. In the γ -mode the thickness of NESCS, d_s, depends on pressure as $d_s \sim p^{-1}$ and it is independent on the frequency. At the middle pressure discharges the magnitude of d_s is $\sim 10^{-2} - 10^{-1}$ cm. As the applied voltage on NESCS does not change remarkably after the mode transition, the contraction of d_s cause sharp increase of the electric field strength.

(ii) Discharge regions following NESCS

Bright region following to NESCS is the negative glow. The field in the negative glow is very weak and thus electrons, which energy is equilibrium with the local field (bulk electrons) are not able to excite/ionize atoms/molecules. In the negative glow the excitation/ionization occurs due to the high energy electrons (fast electrons) invaded from NESCS. After collisions with atoms fast electrons lose their energy and a dark region, the Faraday dark space, arises. Excitation and ionization processes in this region is very limited. The bright region in the middle of the gap is the positive column. The state of plasma in the positive column is independent from the processes occurring in the regions near electrode, it is determined by the local processes. The field is fixed at the value ensuring sufficient ionization which compensates losses of charge carriers and allows closing electric circuit. The length of the positive column is determined by the difference of gap length and the sum of lengths of near electrode layers.

2.2. Excitation and ionization in He

According to [Alves, 1992] in stationary He plasmas there are 9 main groups of elementary processes which control the population of different energy states: excitation / deexcitation by electron collisions, electron impact ionization, radiative transitions, the orbital quantum number change reactions, ionizing reactions between pairs of metastables atoms and atoms in He(2^3P) states, associative ionization, three-body ionic conversion, He ions recombination, diffusion of metastables. In the following these processes are described in detail.

a) Excitation / de-excitation by electron collisions:

$$\mathrm{He}(n,l,s)+\mathrm{e}\underset{k_j^i}{\overset{k_i^j}{\rightleftharpoons}}\mathrm{He}(n',l',s')+\mathrm{e} \qquad (2.1)$$

Here n, l, s are the principal, the orbital and the spin quantum numbers respectively, $i=(n,l,s)<j(n',l',s')$. The cross-sections of reactions (2.1) have been measured and calculated extensively ([Pichou, 1976], [Beigman, 2000]; [Lagus, 1996], [Piech 1997], etc). Depending on the state of reactant and product, four subgroups of the reaction (2.1) are distinguished:

(1) Excitation from the He ground state (direct excitation).
In [Pichou, 1976] the excitation of He (n = 2) was studied changing the electron energy from the threshold value (ε = 19.8 eV) up to 3.6 eV above the threshold. It was found that the cross-section of excitation to the triplet metastable state is remarkably larger than that to the singlet state. The similar result was obtained in [Brongersma, 1972] (ε = 19 - 24 eV), and shown theoretically in [Berrington, 1987] (ε = 19 - 32 eV) and [Obernoi, 1973] (ε = 19 - 23 eV). In [Ashurbekov, 2000] the direct excitation of He(n = 2) states was characterized by empirical rate constant:

$$k=8.71\cdot10^{-6}\frac{\Lambda}{\sqrt{T_\mathrm{e}}\cdot\varepsilon_\mathrm{s}}\exp\left(-\frac{\varepsilon_\mathrm{s}}{T_\mathrm{e}}\right) \qquad (2.2),$$

where ε_s is energy of the state and T_e the electron temperature in eV, $\Lambda=0.03\left(\frac{T_\mathrm{e}}{\varepsilon_\mathrm{s}}\right)^{0.44}$ for $\frac{T_\mathrm{e}}{\varepsilon_\mathrm{s}}\le 0.07$ and $\Lambda=0.25\left(\frac{T_\mathrm{e}}{\varepsilon_\mathrm{s}}\right)^{0.66}$ for $0.07<\frac{T_\mathrm{e}}{\varepsilon_\mathrm{s}}<10$. This formula assumes spin-independent transitions. Comparing direct excitation rate coefficients of singlet and triplet metastable state atoms, this formula predicts higher rate constant to the energetically lower-lying triplet state, He(2^3S).

Experimental and theoretical study of the direct excitation of He(n = 3) states was carried out in [Chutjian, 1975]. At electron energies 29 and 40 eV the calculated cross-sections of He(1^1S-3^3D) transition were larger than that of He(1^1S-3^1D). This result contradicts with experimental finding [John, 1964] and results of more recent theoretical study [Berrington, 1987] where at the electron energy, ε=29 eV, calculated cross-section of He(1^1S-3^1D) transition was ca four times larger than that of He(1^1S-3^3D).

(2) Excitation from metastable He states, 2^1S and 2^3S (stepwise excitation).
In [Piech, 1997] excitation from He triplet metastable was investigated. Metastable atoms were produced in hollow cathode discharge and their density was measured using LIF technology. Atoms in He(2^3S) state were excited to the

He(2^3P, 3^3S, 3^3P, 3^3D, 4^3S, 4^3P, 4^3D, 5^3S, 5^3D) states using a electron gun. Among excitation n = 2 states the largest cross section (peak value $1.2\cdot10^{-14}$ cm^2) was found for transition He(2^3S-2^3P). For states with n > 2, the stepwise excitation of He(n^3S) and He(n^3D) states were more preferred than that of He(n^3P). Study of [Lagus, 1996] where a special attention was paid to eliminate the influence of the ground state atoms, confirmed results of [Piech, 1997] concerning transitions $\mathrm{He}(2^3\mathrm{S}\rightarrow 3^3\mathrm{S},3^3\mathrm{D},4^3\mathrm{D})$.

In [Beigman, 2000] the cross-sections of n = 2, 3 states excitation were calculated using different calculus methods (Born approximation, K-matrix, convergent close coupling). Except Born approximation, other methods gave in the large electron energy diapason for cross-sections of He(2^1S-3^1D) and He(2^3S-3^3D) transitions values which were close to each other.

(3) Transition between He singlet and triplet systems (intercombination transitions).

Transition between singlet and triplet systems may occur due to the electron collisions. The probability of intercombination transitions depends on the energy gap between the corresponding states: it increases when the energy gap diminishes. The early work [Phelps, 1955] showed that spin changing collisions can play a important role. The proposed effective cross-section for transition $\mathrm{He}(2^1\mathrm{S}\rightarrow 2^3\mathrm{S})$ was as large as $\sigma = 3\cdot10^{-14}$ cm^2. In [Mewe, 1970] the rate coefficients of transition between triplet and singlet system were calculated using following formula for cross-sections:

$$\sigma(\varepsilon) = 10^{-16}\cdot c_1\frac{\varepsilon - c_2}{\varepsilon^2} \tag{2.3}$$

Constants for corresponding transitions are given in the table.

Transition	c_1	c_2
$\mathrm{He}(2^1\mathrm{S}\rightarrow 2^3\mathrm{S})$	8.5	0
$\mathrm{He}(2^3\mathrm{S}\rightarrow 2^1\mathrm{S})$	2.8	0.79
$\mathrm{He}(2^1\mathrm{P}\rightarrow 2^3\mathrm{P})$	26	0
$\mathrm{He}(2^3\mathrm{P}\rightarrow 2^1\mathrm{P})$	8.4	0.26

According to the above cited formula and data, the intercombination transitions from the singlet to the triplet states have larger cross-sections than the transitions in the opposite direction.

(4) Superelastic collisions with He metastable atoms

$$\mathrm{He(2S)} + \mathrm{e} \xrightarrow{k_j^i} \mathrm{He}(1^1\mathrm{S}) + \mathrm{e} + \mathrm{KE} \tag{2.4}$$

Here KE is kinetic energy. According to [Deloche, 1976], the rate constant of the reaction is $k_j^i = 4.2 \cdot 10^{-9}\,\mathrm{cm^3 s^{-1}}$.

b) Ionization by electron impact:

$$\mathrm{He}(n,l,s) + \mathrm{e} \xrightarrow{k_i^I} \mathrm{He}^+ + 2\mathrm{e} \tag{2.5}$$

Here k_i^I is the ionization rate coefficient characterizing the electron impact with *i*-state, $(i = (n,l,s))$, atom. Usually only the electron collisions with the atoms in ground and metastable states are taken into account. In the study of the positive column of DC discharge [Mewe, 1970], additionally the electron impact ionization from He(2P) state was considered as a substantial one. In [Mewe, 1970] the cross-sections of reaction (2.5) were calculated according to the equation:

$$\sigma(\varepsilon) = 10^{-16} \cdot c_1 \frac{\varepsilon - c_2}{\varepsilon^2} \ln(c_3 \cdot \varepsilon) \tag{2.6}$$

Constants for corresponding transitions are given in the table.

Transition	c_1	c_2	c_3
$\mathrm{He}(1^1\mathrm{S}) \rightarrow \mathrm{He}^+$	29	24.6	0.056
$\mathrm{He}(2^1\mathrm{S}) \rightarrow \mathrm{He}^+$	88	4.0	0.35
$\mathrm{He}(2^3\mathrm{S}) \rightarrow \mathrm{He}^+$	73	4.8	0.29
$\mathrm{He}(2^1\mathrm{P}) \rightarrow \mathrm{He}^+$	103	3.4	0.41
$\mathrm{He}(2^3\mathrm{P}) \rightarrow \mathrm{He}^+$	96	3.6	0.38

c) Radiative transitions

$$\mathrm{He}(n,l,s) \xrightarrow{A} \mathrm{He}(n',l \pm 1,s) + h\nu \tag{2.7}$$

Here A – the probability of radiative transition, $(n,l,s) > (n',l \pm 1,s)$.

Figure 2 presents a schematic energy level diagram with selected radiative transitions. The probabilities of radiative transitions presented in the figure 2 are given in the table 1.

Table 1. Radiative transition probabilities, A of selected spectral lines [Ralchenko, 2008].

Tran-sition	λ, nm	ε_s, eV	A, s^{-1}	Tran-sition	λ, nm	ε_s, eV	A, s^{-1}
2^1P-1^1S	58.4	21.22	$1.8\cdot10^9$	3^1P-2^1S	501.5	23.09	$1.3\cdot10^7$
4^3P-2^3S	318.8	23.71	$5.1\cdot10^6$	3^3D-2^3P	587.6	23.07	$7.1\cdot10^7$
3^3P-2^3S	388.9	23.01	$9.5\cdot10^6$	3^1D-2^1P	667.8	23.07	$6.4\cdot10^7$
4^1P-2^1S	396.5	23.74	$7.2\cdot10^6$	3^3S-2^3P	706.5	22.72	$1.5\cdot10^7$
4^3D-2^3P	447.1	23.74	$2.5\cdot10^7$	3^1S-2^1P	728.1	22.92	$1.8\cdot10^7$
4^3S-2^3P	471.3	23.59	$1.2\cdot10^6$	2^3P-2^3S	1082.9	20.96	$1.0\cdot10^7$
4^1D-2^1P	492.2	23.74	$2.0\cdot10^7$	2^1P-2^1S	2058.7	21.22	$2.0\cdot10^7$

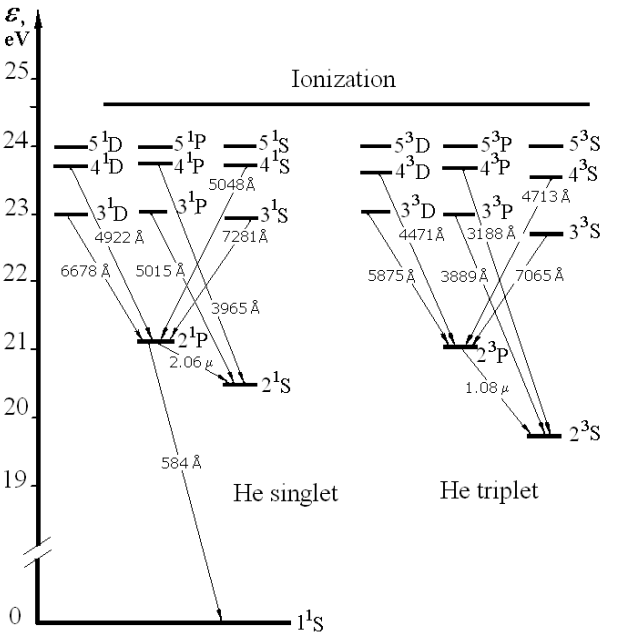

Figure 2. Schematic energy level diagram with selected radiative transitions [Alves, 1991].

According to the table 1 the probability of radiative transition He(2^1P-1^1S), $\lambda = 58.4$ nm, has the highest value, $A_{58} = 1.8\cdot10^9\ s^{-1}$.

d) The orbital quantum number change reactions:

$$\mathrm{He}(n,l,s) + \mathrm{He}(1^1\mathrm{S}) \underset{k_j^i}{\overset{k_i^j}{\rightleftarrows}} \mathrm{He}(n,l',s) + \mathrm{He}(1^1\mathrm{S}) \qquad (2.8)$$

Here $i = (n,l,s) > j = (n,l',s)$. The cross-section of reaction (2.8) depends on energy gap $\Delta\varepsilon = \varepsilon_{s\_i} - \varepsilon_{s\_j}$ separating i -and j sublevels (figure 3).

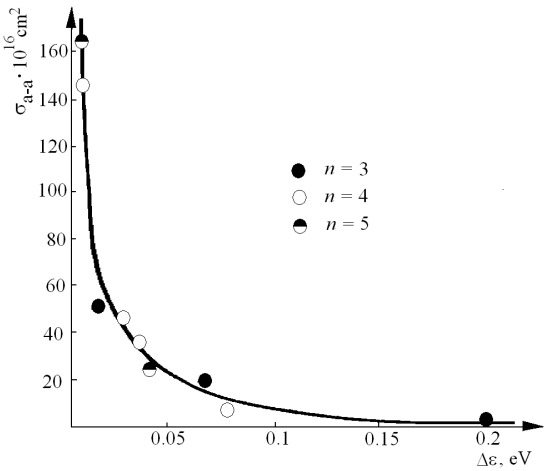

Figure 3. Cross-section of reaction (2.8) as a function of energy difference, $\Delta\varepsilon = \varepsilon_{s\_i} - \varepsilon_{s\_j}$. [Pavlovskaja, 1973].

If the gas temperature T_g is higher than $\Delta\varepsilon$ then according to [Alves, 1992] the empirical expression of the *l*-changing de-excitation rate coefficient could be written as:

$$k_i^j = 7.76 \cdot 10^{-10} \left(\frac{\Delta\varepsilon}{T_g} \right)^{-0.29} \frac{1}{g_i} \tag{2.9}$$

Here g_i - statistical weight of *i*- state.

e) Ionization in reactions between pairs of metastables atoms and atoms in He(2^3P) states:

$$\begin{aligned} \mathrm{He}(n,l,s) + \mathrm{He}(n',l',s') &\xrightarrow{k_{i,j}\cdot\xi} \mathrm{He}(1^1\mathrm{S}) + \mathrm{He}^+ + \mathrm{e} \\ &\xrightarrow{k_{i,j}\cdot(1-\xi)} \mathrm{He}_2^+ + \mathrm{e} \end{aligned} \tag{2.10}$$

Here ξ - branching ratio, $i = (n,l,s)$, $j = (n',l',s')$.

In an early work [Roos, 1959] an extremely small cross-section of reaction (2.10) was calculated ($\sigma \sim 10^{-18}$ cm^2) and a weak temperature dependence of σ was found. Despite of small σ in [Myers, 1963] was suggested that at low pressure afterglow the main He ionization channel is mutual collision of He metastable atoms. Drastically larger cross-section of reaction (2.10) (as reactants were two He(2^3S) atoms) was calculated in [Garrison, 1973]: at room

temperature $\sigma \approx 10^{-14}$ cm^2. They found also strong dependence of branching ratio on the gas temperature (figure 4 A). Branching ratio $\xi = 0.30 \pm 0.05$ was suggested in [Deloche, 1976]. Calculations showed that He_2^+ produced in reaction (2.10) is at high vibrational states (v>10, figure 4 B).

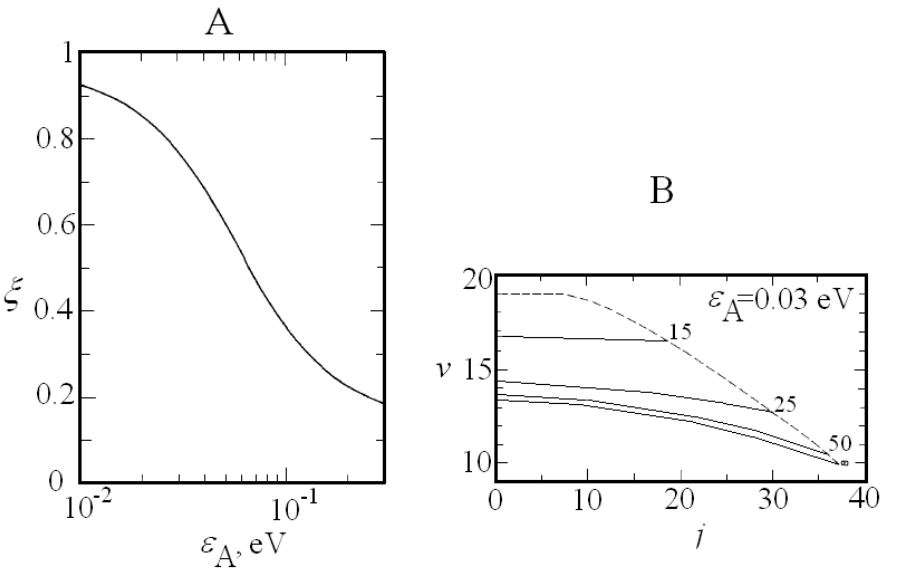

Figure 4. A- Branching ratio, ξ, as a function of relative collision energy ε_A. B- distribution of vibrational (v) and rotational (*j*) states for cross-sections forming molecule in particular vibrational-rotational state, $\sigma = (15, 25, 50) \cdot 10^{-4}$ Å^2. ε_A=0.03 eV. [Garrison, 1973].

Large cross-section was also obtained in the experimental study of middle pressure afterglow discharge, $\sigma \approx 3 \cdot 10^{-14}$ cm^2 [Johnson, 1973]. Recent EEDF probe measurements of a low pressure afterglow discharge [DeJoseph, 2007] confirmed high rate of reaction (2.10): in EEDF was detected peak value at energy ε=14.4 eV which arises according to [Demidov, 1991] as a result of reaction (2.10). However, modelling [Kutasi, 2001] of He pulsed discharge showed relatively low importance of this kind of ionization mechanism (despite quite high metastable concentration, [He_m]~10^{12} cm^{-3}): in the pressure range of 5 - 46 Torr only $\approx$ 10 % of overall ionization acts occurred via reaction (2.10).

f) Associative ionization (Hornbeck-Molnar process):

$$\mathrm{He}(n,l,s)+\mathrm{He}(1^1\mathrm{S})\xrightarrow{k_i^I}\mathrm{He}_2^+ + \mathrm{e} \tag{2.11}$$

Large number of collisions occurs between metastable and ground state He atoms but only a very small fraction of He atoms in the low temperature plasmas have sufficient translational energy to ionize metastable He atoms.

g) Three-body ionic conversion

$$\mathrm{He}^+ + 2\mathrm{He}(1^1\mathrm{S}) \xrightarrow{k_{\mathrm{konv}}} \mathrm{He}_2^+ + \mathrm{He}(1^1\mathrm{S}) \tag{2.12}$$

This process is expected to be an important He_2^+ production channel at higher operating pressures: according to [Deloche, 1976] at pressures $p > 5$ Torr the dominant ion in He discharges is He_2^+. The empirical formula for calculation of k_{konv} is proposed in [Böhringer, 1983]:

$$k_{\mathrm{konv}} = 1.4\cdot 10^{-31}\left(\frac{T_{\mathrm{g}}}{300}\right)^{-0.6} \tag{2.13}$$

According to the modeling results of [Kutasi, 2001] at middle pressure discharge (p~50 Torr) the three body ionic conversion is the main channel producing ions He_2^+.

h) He^+ and He_2^+ recombination

(1) recombination of He^+.
According to [Emmert, 1988], the recombination of He^+ populates He(2S, 2P) states in reaction:

$$\mathrm{He}^+ + 2\mathrm{e}\xrightarrow{k_{\mathrm{S}}}\left\{\begin{array}{l}\mathrm{He}\left(2^1\mathrm{P}\right)+\mathrm{e},\ 19\%\\ \mathrm{He}\left(2^1\mathrm{S}\right)+\mathrm{e},\ 6\%\\ \mathrm{He}\left(2^3\mathrm{P}\right)+\mathrm{e},\ 56\%\\ \mathrm{He}\left(2^3\mathrm{S}\right)+\mathrm{e},\ 19\%\end{array}\right\} \tag{2.14}$$

Here the branching ratio is given in percentages. In an earlier work [Hinnov, 1962] it was found that the rate coefficient k_{s} depends on the electron temperature as $k_{\mathrm{s}} \propto T_{\mathrm{e}}^{-9/2}$. According to [Emmert, 1988] coefficient k_{s} could be express as

$$k_s = 6.0 \cdot 10^{-20} \left(\frac{0.025}{T_e} \right)^4 \qquad (2.15).$$

(2) recombination of molecular ion He_2^+

Most of works dedicated to He_2^+ recombination are performed in afterglow discharge conditions where it in generally has been recognized as a process with very low rate coefficient.

He_2^+ recombination occurs either in two or three body reactions. Two body recombination, direct dissociative recombination occurs in reaction:

$$He_2^+ + e \xrightarrow{k_{DR}} He(n,l,s) + He\left(1^1S\right) + E_D \qquad (2.16)$$

Here E_D marks kinetic energy. Dissociative recombination requires the crossing of potential curves of molecular ion with curve of the repulsive neutral-molecular one. In the case of He_2^+ the curve crossings occurs at vibrational states $v \geq 3$ (figure 5). Dissociative recombination can be efficient only if it is exothermic [Rogers 1964], i.e. transition from bound state to the dissociated state must be accompanied by the conversion of potential energy into kinetic energy, E_D.

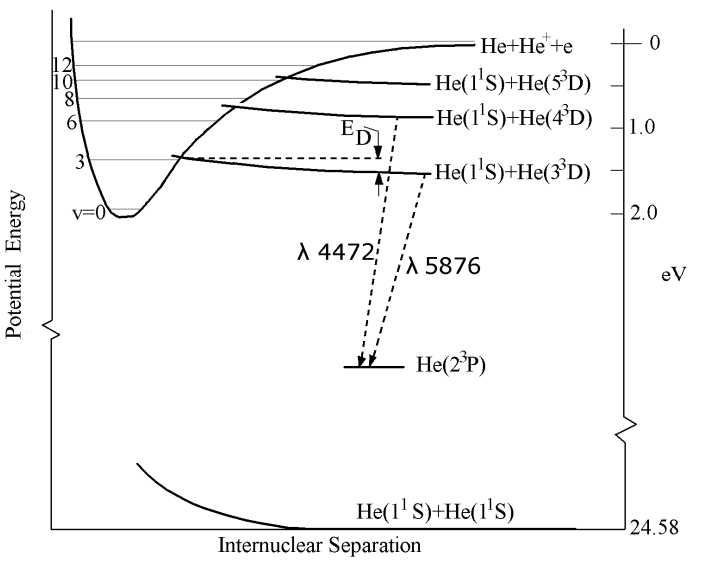

Figure 5. Schematic representation of potential curves of He_2^+ and quasi-molecule $He(1^1S)+He^*$ [Rogers 1964].

The kinetic energy E_D is sheared between the fragments which fly out from the dissociating system. For homonuclear diatomic molecule this energy is sheared equally between two atoms. In the case of He the relative energies of the molecular-ion ground state and the molecular and atomic states are such that one of the atoms will almost certainly be produced in an electronically excited state. If the atom does not lose obtained kinetic energy due to collisions with other particles before radiating, the emitted photon will be shifted from its normal wavelength because of the Doppler effect. Since there is no preferred direction for dissociation, Doppler broadening of a spectral line takes place. In [Rogers, 1964] dissociative recombination of low pressure afterglow was studied. Experimentally detected broadening of $\lambda = 587.6$ nm spectral line (transition 3^3D-2^3P) during the afterglow was explained by Doppler effect and it was taken as a proof of He(3^3D) state excitation via dissociative recombination.

In afterglow study [Ivanov, 1983] intensity dependences of He atomic lines on the electron temperature and the post pulse time was investigated. Intensity dependence on electron temperature indicated on two different excitation paths of He states. Density of n = 3,4 He states depend on T_e weakly, $\left[\mathrm{He}(n=3,4)\right] \propto T_e^{-0.5}$ and the proposed population mechanism of these states was dissociative recombination. The conclusion was supported by growth of ratio of intensities of lines λ=667.8 nm (transition 3^1D-2^1P) and λ=492.2 nm (4^1D-2^1P) with postpulse time. Presuming that higher He states are populated from less populated upper He_2^+ vibrational levels, growth of the ratio was explained with vibrational relaxation of He_2^+. For state He(2^3P) dependence on electron temperature was stronger, $\left[\mathrm{He}(2^3\mathrm{P})\right] \propto T_e^{-1.5}$. Intensity dependence of He_2 molecular bands and spectral line $\lambda = 1083.0$ nm (2^3P-2^3S) on electron temperature was similar. Therefore authors proposed He(2^3P) population via intermediate excited He_2^* molecule in three body reaction $\mathrm{He}_2^+ + \mathrm{e} + \mathrm{He} \rightarrow \mathrm{He}_2^* + \mathrm{He} \rightarrow \mathrm{He}^* + 2\mathrm{He}$.

More detailed treatment about He_2^+ recombination is given in theoretical work [Carata, 1999]. In this work two recombination mechanisms- direct and indirect is distinguished. The direct process marks dissociative recombination when electron is captured directly into dissociative state. In the case of indirect process electron is first captured into Rydberg state of He_2^* which then is transferred by electronic interaction to the dissociative state. It was showed that cross-section of dissiciative recombination depends strongly on initial vibrational state of He_2^+. The cross-section depends also on electron energy, e.g. for $He_2^+(v=3)$ increase of electron energy from 0 to 1 eV causes decrease of the cross-section from $\sim 10^{-14}$ to 10^{-16} cm^2. It was found that dissociation of three lowest dissociative states of excited He_2 populate He(2^1S, 2^3S, 2^3P) states.

In [Pedersen, 2005] dissociative recombination of $^4He_2^+$ isotopomer $^3He^4He^+$ was studied in storage ring experiment. Similarly to [Carata, 1999] it was found that dissociative recombination depends strongly on the initial vibrational state of the ion: the rate of dissociative recombination from He_2^+ states $v \geq 3$ was ca

three order of magnitude higher than from $v < 3$. According to measurements recombination from $v < 3$ states populates first of all He(2^3P) and He(2^1S) states (from $v = 0$ ca 59% of recombination lead to He(2^3P) and 37% to He(2^1S)). It was concluded that dissociative recombination from He_2^+ states $v \geq 3$ leads into higher lying atomic states avoiding the $n = 2$ final state.

In storage ring study [Urbain, 2005] both dissociative recombination of $^4He_2^+$ and $^3He^4He^+$ were studied. Because of negligible vibrational decay, homonuclear $^4He_2^+$ was used for the investigation of recombination from higher He_2^+ vibrational levels. It was found that the cross-section of $^4He_2^+$ recombination diminishes monotonically with increasing electron energy: at electron energy ε = 0.001 eV, $\sigma_{DR} \sim 10^{-13}$ cm^2 while for ε = 1 eV $\sigma_{DR} \sim 10^{-15}$ cm^2. From cross-section measurements it was deduced the dissociative recombination rate coefficient for higher vibrational states:

$$k1_{DR} = 1.23 \cdot 10^{-7} \left[\frac{300}{T_e} \right]^{\frac{1}{2}} \tag{2.17}$$

The recombination rate coefficient for ground vibrational state, deduced on the basis of $^3He^4He^+$ recombination cross-section measurements, was in good agreement with results of the afterglow studies: $k2_{DR} = 6 \cdot 10^{-10}$ cm^{3}s^{-1}.

According to [Deloche, 1976], He_2^+ is always, independently from production mechanism, form at high vibrational states ($v \geq 10$). The rate of dissociative recombination depends strongly on vibrational state of recombining ion ([Carata,1999, [Pedersen, 2005], [Urbain, 2005]), i.e. on the rate of vibrational relaxation. In theoretical work [Bates, 1979] two vibrational relaxation mechanisms is proposed: (1) relaxation due to the exothermic reaction

$$He_2^+(v) + He(1^1S) \rightarrow He_2^+(v - \delta) + He(1^1S) \tag{2.18}$$

and (2) relaxation due to three body recombination into a Rydberg state $He_2^+(v) + e + e \rightarrow He_2(v,n) + e$ followed by the autoionization $He_2(v,n) \rightarrow He_2^+(v-1) + e$. For reaction 2.18 [Bates, 1979] considered rate coefficient $k_{VR} = 1 \cdot 10^{-10}$ cm^{3}s^{-1} while according to the estimation given in the experimental work [Ivanov, 1988] $k_{VR} < 10^{-14}$ cm^{3}s^{-1}.

Three body recombination of He_2^+ may take place in two different ways [Emmert, 1988]:

(1) reaction with two electrons leads to highly excited molecule He_2^{**},

$$He_2^+ + 2e \rightarrow He_2^{**} + e \tag{2.19}$$

which either dissociate

$$He_2^{**} + He(1^1S) \rightarrow He^* + 2He(1^1S) \tag{2.20}$$

or are de-excited to $He_2^*(A)$ or $He_2^*(a)$:

$$\begin{aligned} He_2^{**} + e &\rightarrow He_2^*(A) + e \\ &\rightarrow He_2^*(a) + e \end{aligned} \tag{2.21}$$

$He_2^*(A)$ decays by radiation to the repulsive ground state while $He_2^*(a)$ is a metastable.

As efficiency indicator of reactions (2.19–2.21) serves molecular florescence of He_2.

(2) reactions with one electron and one He atom transfers He_2^+ into He(2P):

$$He_2^+ + e + He(1^1S) \rightarrow He(2P) + He(1^1S) \tag{2.22}$$

The excitation mechanism of this reaction product, He(2P), has been subject of numerous afterglow studies. In [Collins, 1969] strong dependence of $He(2^3P)$ population on the excited He_2 population was observed. From this finding authors concluded that $He(2^3P)$ is populated via reaction (2.22). In high pressure study (excitation by electron beam) [Emmert, 1988] the He_2^+ recombination in the reaction (2.22) was clarified and rate constants for reactions leading to singlet ($k = 1.8 \cdot 10^{-31}\,cm^6s^{-1}$) and triplet ($k = 1.6 \cdot 10^{-32}\,cm^6s^{-1}$) He states were deduced.

i) Diffusion of metastables

Depending on experimental conditions diffusion losses of He metastable states atoms towards to the walls of the container could be became significant loss mechanism of He metastable atoms. In the afterglow study [Deloche, 1976] evaluated diffusion coefficient for He metastables is connected with the diffusion coefficient at standard conditions ($N_0 = 3.5 \cdot 10^{16}\,cm^{-3}$, $T_0 = 293\,K$) as

$$D = D_0 \cdot \frac{N}{N_0} \sqrt{\frac{T_g}{T_0}} \tag{2.23}$$

Here N is density of He atoms. For He(2^3S) $D_0 = 420\ \mathrm{cm^2 s^{-1}}$.

In a cylindrical plasma column the diffusion time τ is obtained using Besselian radial distribution of metastable concentration [Dothan, 1981]:

$$\frac{1}{\tau} = D \cdot \frac{5.8}{R^2} \tag{2.24}$$

Here R- tube radius (cm).

2.3. Ionization of N_2 in He / N_2 mixture

Several experiments have shown that addition of some amount of N_2 to He have strong influence on the spectral characteristics of the discharge. Because of molecular structure and significantly lower ionization potential of nitrogen, one could expect change of electron energy distribution function (EEDF) and ionization path compared with situation in the case of pure He. In the mixture of He / N_2 at low N_2 concentration usually two helium-nitrogen interaction mechanisms are discussed: Penning reaction,

$$\mathrm{He}(2^3\mathrm{S}) + \mathrm{N_2} \xrightarrow{k_\mathrm{P}} \mathrm{N_2^+} + \mathrm{He}(1^1\mathrm{S}) + \mathrm{e} \tag{2.25}$$

and charge transfer reactions:

$$\mathrm{He_2^+} + \mathrm{N_2} \xrightarrow{k_{\mathrm{CT1}}} \mathrm{N_2^+} + 2\mathrm{He}(1^1\mathrm{S}) \tag{2.26}$$

$$\mathrm{He^+} + \mathrm{N_2} \xrightarrow{k_{\mathrm{CT2}}} \mathrm{N_2^+} + \mathrm{He}(1^1\mathrm{S}) \tag{2.27}$$

According to [Hotop, 1970] Penning reaction populates the three lowest electronic states of N_2^+: X, A, and B in the proportions of 35, 24, 41 correspondingly. The vibrational population of N_2^+(X) and N_2^+(B) state are found to be in agreement with those expected from Frank-Condon factors [Schmeltekopf, 1968]. In the case of Penning reaction the rotational temperature of N_2^+(B, v=0) state corresponds about to the N_2(X) i.e. to the gas temperature ([Belikov, 1997], [Endoh, 1983]). The rate coefficients of Penning reaction found in different studies are relative close each other varying from $6 \cdot 10^{-11}$ to $8 \cdot 10^{-11}$ $\mathrm{cm^3 s^{-1}}$ ([Märk, 1971], [Pouvesle, 1982], [Schmeltekopf, 1970]).

The charge transfer reactions, particularly with atomic ions He^+ lead to the electronic, vibrational and rotational populations different from those of Penning reaction. The state of products depends on recombination energy of corresponding helium ion [Leventhal, 1975]. The lower limit of recombination energy of He^+ ion is fixed at 24.6 eV and thus reaction (2.27) populates higher N_2^+ states: most of products are in N_2^+(C) state and only ~ 10 % are in N_2^+(B) state [Farragher, 1970]. Rate coefficients of reaction (2.27) vary in different studies from $1 \cdot 10^{-9}$ to $1.7 \cdot 10^{-9}$ $cm^3 s^{-1}$ ([Pouvesle, 1982], [Fehsenfeld, 1966], [Dunkin, 1968], [Schmeltekopf, 1968], [Warneck, 1967]).

Reaction with He_2^+, (2.26), populates mainly N_2^+(B) state as He_2^+ recombination energy lies in the range 18.3–20.3 eV (figure 6) with maximum probability at about 19.3 eV, i.e. resonant with low vibrational levels of N_2^+(B) [Leventhal, 1975].

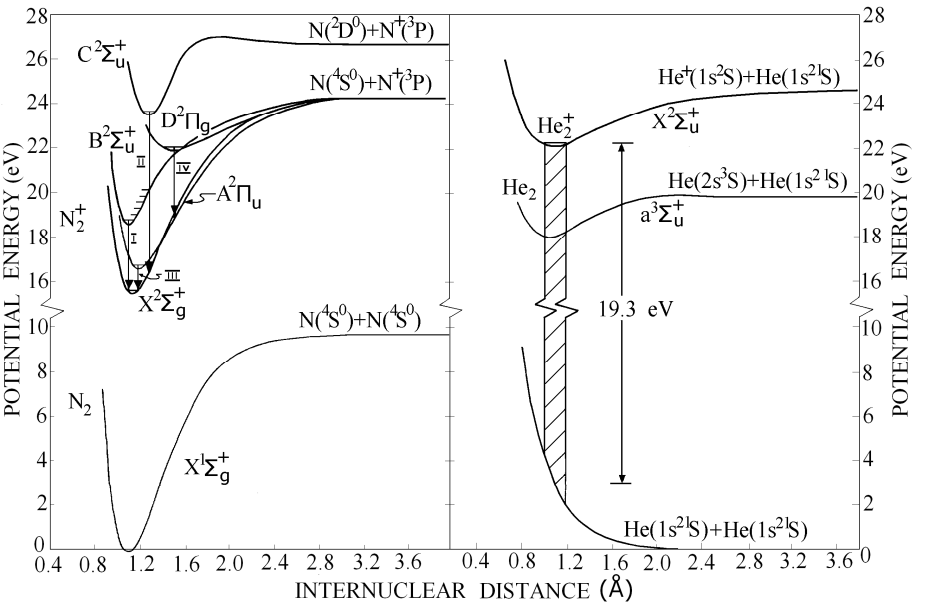

Figure 6. Potential curves for N_2, N_2^+, He_2, He_2^+ and repulsive He-He potential. N_2^+ band systems: I – B-X (first negative), II – C-X (second negative), III – A-X (Meinel), IV – D-A (Janin-d'Incan). [Leventhal, 1975].

According to [Endoh, 1983] the rotational population of N_2^+(B) produced by reaction (2.26) corresponds to the thermal equilibrium distribution at about 900 K. The rate coefficient for reaction (2.26) varies from $6 \cdot 10^{-10}$ to $1.1 \cdot 10^{-9}$ $cm^3 s^{-1}$ ([Fehsenfeld, 1966], [Lee, 1976], [Pouvesle, 1982]).

In some studies of He / N_2 discharge additionally to (or instead of) Penning and charge transfer reactions other N_2 ionization mechanisms are considered. In

the theoretical study of atmospheric pressure HF discharge [Petrof, 2000] it was found that despite low N_2 concentration Penning and charge transfer reactions are of negligible importance and ionization of nitrogen atoms and molecules occurs mainly due to electron impact with nitrogen. In low pressure afterglow study [Märk, 1971] N_2 ionization in reactions between N_2 excited spices was considered.

2.4. Research program

Current work deals with two main problems:

(I) The first problem concerns the recombination path of the He molecular ion. According to the literature review, most of works where He_2^+ recombination is investigated, are afterglow studies. In afterglow discharges ions He_2^+ are mostly at lower vibrational states and therefore the recombination rate coefficient is low.

In the case of stationary discharge, which is the subject of present investigation, the population of higher vibrational states of He_2^+ should be remarkably higher. Recent storage ring studies showed that in the case of high vibrational excitation, He_2^+ recombination could be a very efficient populating mechanism of He states.

The main task of the research program is to develop a method, which allows to distinguish the contribution of different excitation mechanisms of He. Comparison of discharges of negative glow and positive column regions where the excitation mechanisms differ drastically, should give answer to the problem.

(II) Another problem is connected with the N_2 ionization mechanism in He / N_2 discharge. According to the literature review in studies of He / N_2 mixtures at low N_2 concentration mainly two ionization mechanisms- Penning and charge transfer reactions are considered.

To determine relative importance of these reactions, concentrations of He_2^+ and He metastable state atoms as function of N_2 fraction should be determined.

3. EXPERIMENTAL SETUP AND PROCEDURE

3.1. Capillary tube

Two capillary tubes were used: quartz (SiO_2, bore diameter $d = 3$ mm) and ceramic (Al_2O_3, $d = 2$ mm) ones. The length of both tubes was $L_c = 310$ mm and the wall thickness 1 mm.

During the first measurements the quartz tube was used as its walls were transparent in a wide region of spectrum. However it appeared that because of sputtering of walls material the gas polluted quickly. According to [Reich, 1994] sputtering yield of ceramic is more than 7 times less than that of quartz. Therefore the quartz tube was replaced by a ceramic one. The other advantage of ceramic is ca 8 times higher thermal conductivity than that of quartz (Lide, 1997). At the same time the walls of the ceramic tube were light scattering which did not allowed to record the light distribution along the tube diameter. According to experimentally determined relative transmittance, tube walls were opaque at wavelength $\lambda < 500$ nm. For $\lambda > 700$ nm the transparency of the walls did not depend on wavelength.

3.2. Vacuum / gas handling system

Sketch of the vacuum / gas handling system is presented in figure 7. The system was designed using materials with low degassing values: metal (pipes, mixing volume) and glass (pipes). ERTA PEEK (polyetheretherketone) was used in construction of capillary holder. For sealing Viton O rings were used.

The pressure in the system was determined by Wenzel A200 Gauge System and ionization gauge VIT-2. Wenzel A200 Gauge System contained two sensors, (both the same type, Wenzel Dualtrance) which measure pressure in the range $1 \cdot 10^{-5}$ – 4000 Torr. Gauge VIT-2 measure pressure in the range 10^{-3} - 10^{-7} Torr.

The system was evacuated by mechanical and diffusion pumps. To avoid oil vapour migration to high purity system, between the system and pumps were set oil traps: for mechanical pump a silica gel filter, for diffusion pump a liquid nitrogen cooled trap. To ensure efficient removal of residual gases it was possible to heat the system up to ≈ 80 °C. The minimum residual pressure achieved was $1 \cdot 10^{-6}$ Torr.

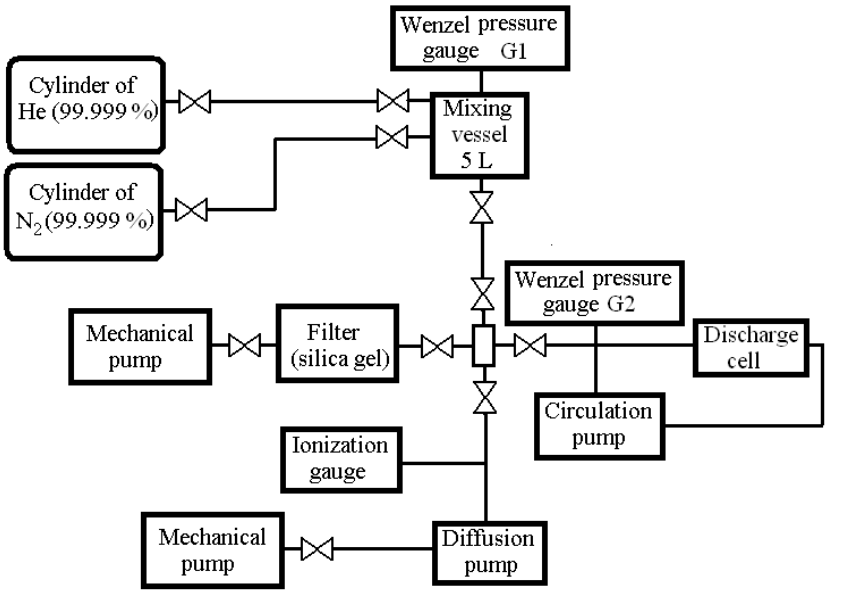

Figure 7. Sketch of the vacuum / gas handling system.

He and N_2 of 99.999% purity were used for preparing of gas mixtures. Diffusive mixing of gases in the mixing vessel lasted at least 5 min. Then mixture was introduced into discharge volume. Circulation of the gas in the system was provided by the circulation pump. From outside the capillary was cooled by an air blowing fan and in the case of negative glow studies the grounded electrode was cooled by flowing tap water.

As discharge in helium is very sensitive to impurities, every recording of the spectrum was carried out in a fresh gas. Before a new filling, the whole system was evacuated to a pressure less than 10^{-5} Torr.

3.3. System of electrical measurements and arrangements of electrodes

The electrical system schematic is shown in figure 8. A generator UVZ-80-3 of 27 MHz frequency and of 130 W maximum output power excited the discharge. Homemade Rugowski coil (designed by Dr. M. Aints) was used for current measurements. Voltage was measured with capacitive voltage divider constituted from capacitors C_1, C_2. Voltage and current were registered with analogue oscilloscope C1-99. For phase shift measurements a digital oscilloscope Velleman PC5500 was used. The discharge was excited between two electrodes, one of which (powered electrode) was connected via matching capacitor C_M with the generator, another was grounded through Rugowski coil.

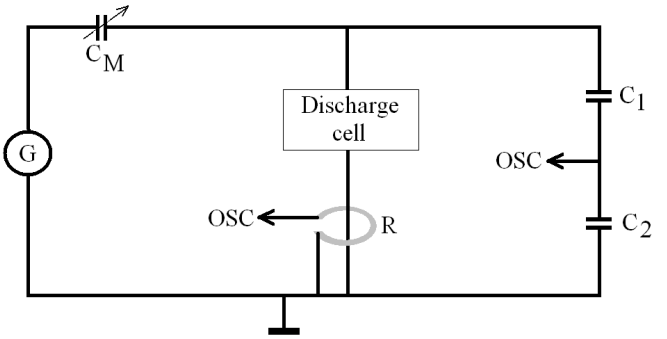

Figure 8. Electrical schema. G- generator C_M- matching capacitor, R- Rugowski coil, C_1, C_2 voltage dividing capacitors, OSC – oscilloscope.

Two different electrode configurations was used (figure 9).

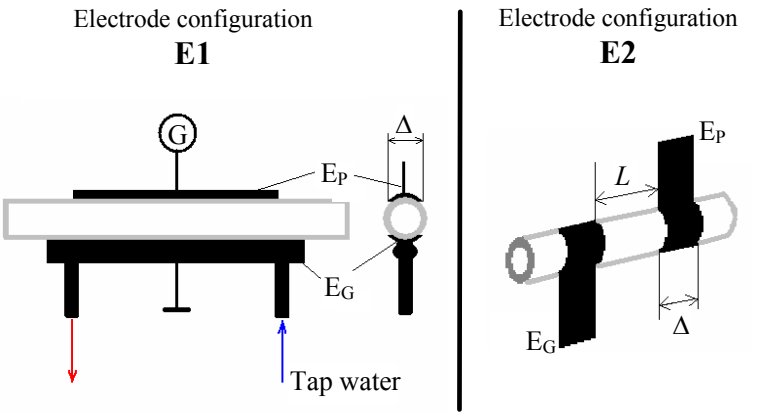

Figure 9. A sketch of electrode configurations E1 and E2.

In the study of negative glow region electrode configuration E1 was used. The width of both electrodes, Δ, was 2.5 mm. The length of the powered electrode, E_P, was 190 mm. The grounded electrode, E_G, of 196 mm length was cooled by tap water.

Electrode configuration E2 was used in the study of positive column region. The voltage was applied to the metal straps, which enveloped the capillary. The width of straps was $\Delta = 14$ mm. The distance between electrodes, L, was changeable but most of the experiments were carried out at the distance $L = 34$ mm.

3.4. System of optical measurements

A sketch of spectrum measurement setup is shown in figure 10.

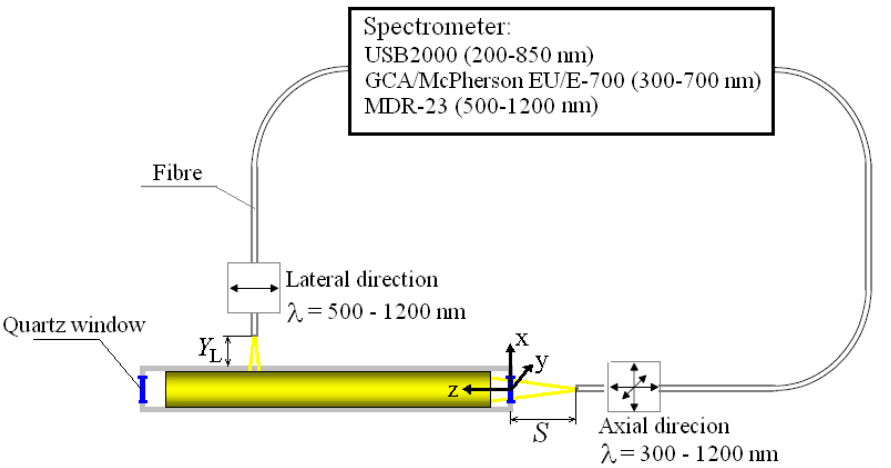

Figure 10. Sketch of spectrum measurement setup.

The spectrum was recorded using three different spectrometers. Fibers guided the light to the spectrometers. Spectrum measurements were carried out mainly with Ocean Optics USB2000 spectrometer which recorded the spectrum in 200 - 850 nm range. Experimentally determined resolution of the spectrometer was 1.5 nm. The integration time was changed from 300 to 1000 ms. The relative spectral sensitivity was determined using the tungsten halogen lamp of calibrated spectral distribution, figure 11.

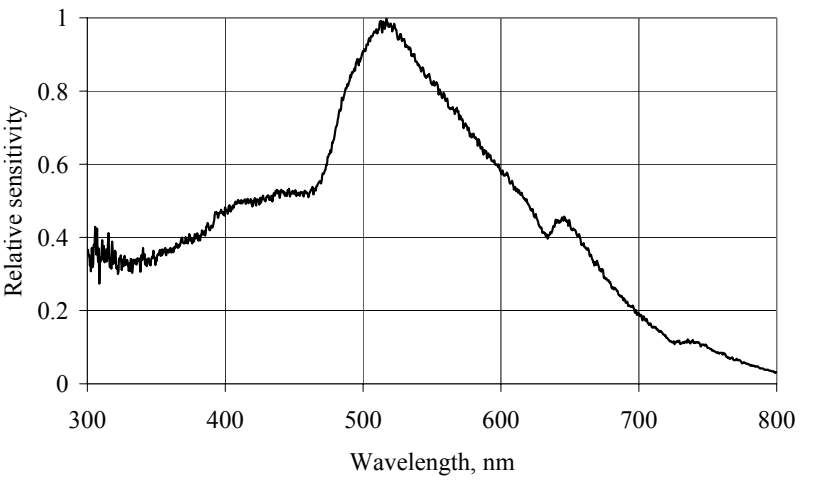

Figure 11. Relative spectral sensitivity of USB2000 spectrometer.

In 300–700 nm region some parts of the spectrum were recorded by the GCA/McPherson EU/E-700 spectrometer (grating: 1200 grooves per mm) with Hamamatsu 1P28 PMT. The spectrometer MDR-23 (600 grooves per mm) with FEU-62 PMT was used in the 700 - 1200 nm spectral region.

3.5. Adjustment of optical system

The spectrum was recorded both in the lateral and axial directions.

Construction of the fibre holder allowed smooth movement end of the fibre in three directions. When recording the intensity distribution in the plane, which was perpendicular to the capillary axis, the distribution depended on the distance S between the plane and the capillary end as well as on the distance Z between the plasma column and the end of the capillary. Figure 12 gives the intensity distribution of He 587.6 nm line recorded for He plasma (p=60 Torr; i = 0.07 A): it appeared that instead of expected maximum at (x,y)=(0,0) there was a local minimum.

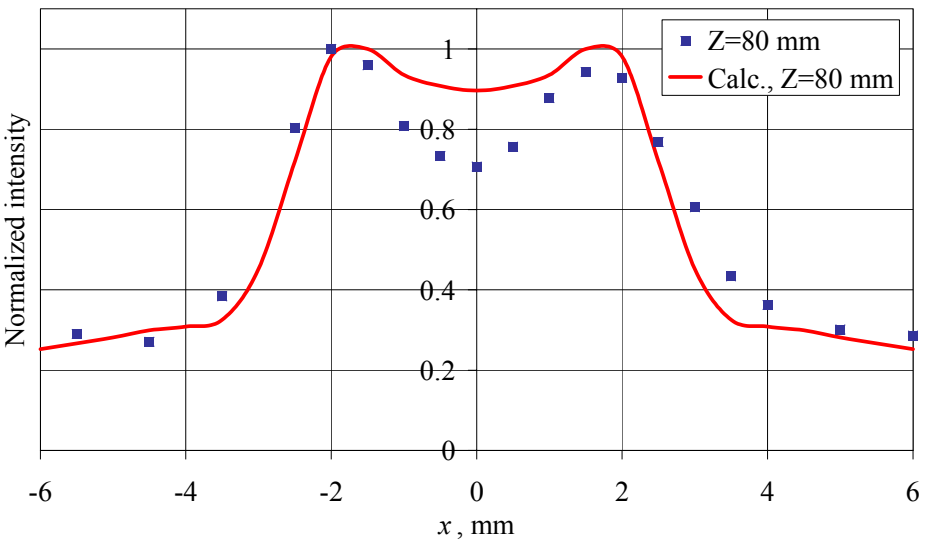

Figure 12. Measured (points) and calculated (line) intensity distributions as a function of fibre position in the x-axis; S=200 mm; the length of the discharge column is 20 mm.

The appearance of the minimum at the centre of the distribution becomes understandable considering that at a distance S, the intensity distribution at the plane F depends on (1) the light falling directly on the plane, I_D, and (2) the light falling on the plane after reflection from the capillary walls, I_R, (figure 13).

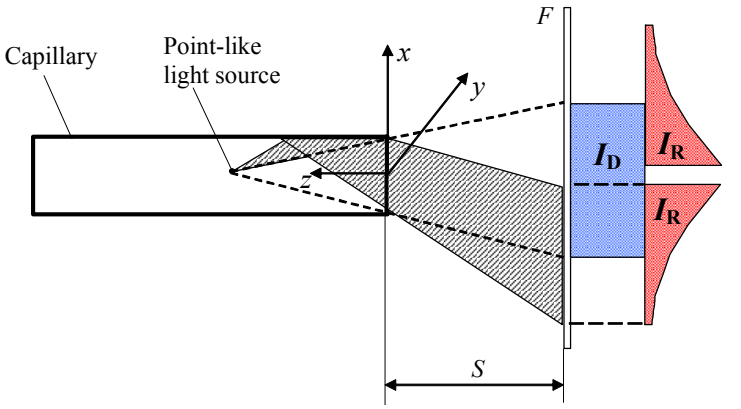

Figure 13. Schematic representation of the light distribution formation along *x*-axis when $Z / S < 1$.

Let the point-like light source is at a distance Z from the end of the capillary and the intensity distribution is measured along *x*-axis at the plane F, which is at distance S, figure 13. Directly falling light causes more-or-less homogeneous intensity distribution, I_D. At the same time, the intensity distribution caused by the reflected light depends on ratio Z / S and on the reflection coefficient. When the ratio $Z / S < 1$, like in figure 13, in the region near $x = 0$ the intensity of the reflected light $I_R = 0$, and at the centre of the summary distribution there is a dip. In figure 12 is shown measured and calculated distributions for ratio, $Z / S < 1$. In calculations only single reflections from the capillary wall were taken into account, reflection coefficients for Al_2O_3 (λ = 590 nm) were taken from http://reflectioncoefficient.info/index.php?group=CRYSTALS&material=Al2O3. The discrepancy of measured and calculated distributions is likely caused by assumption that plasma fills the capillary cross-section homogeneously. Increasing the Z / S ratio leads to the decrease of the dip and at $Z / S > 1$ the intensity maximum is positioned at the centre of the distribution.

Carrying out the spectral measurements, the fibre end was positioned at such a distance S where the condition $Z / S > 1$ was fulfilled for all Z occupied by plasma column.

Recording spectra from the lateral direction, the fibre tip was positioned at the distance Y_L from the capillary wall where the intensity of non-absorbed He spectral lines at wavelength $\lambda > 700$ nm was equal to the intensity recorded in the axial direction.

4. RESULTS AND DISCUSSION

4.1. Discharge appearance

The discharge light distribution between electrodes was measured from the lateral direction of the capillary.

The light distribution along the capillary diameter was possible to determine only using the quartz tube. Figure 14 presents the distribution in the case of electrode configuration E1 recorded by CCD camera.

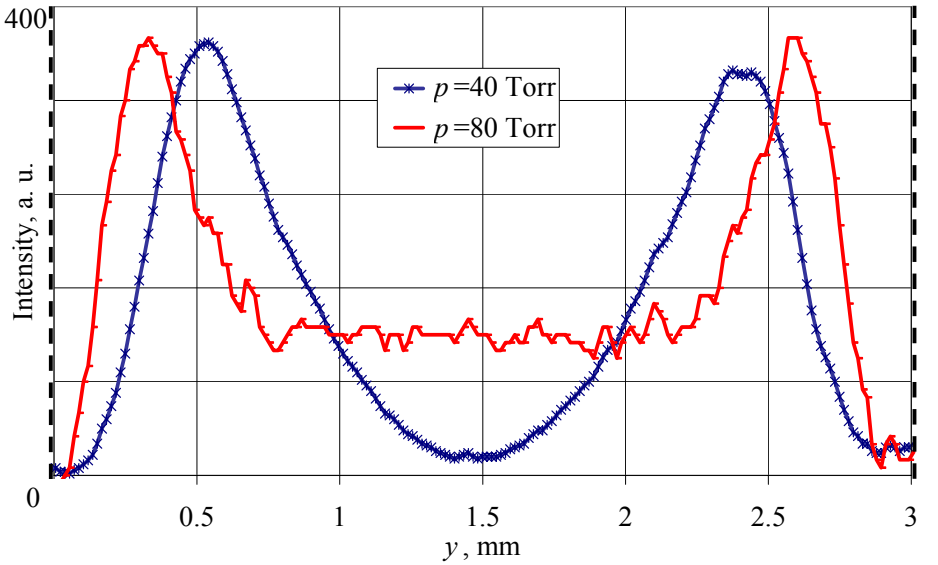

Figure 14. Lateral light distribution in He, i = 0.25 A. Vertical dashed lines mark the inner walls of the tube. Electrode configuration E1.

The light distribution was almost symmetrical relative to the capillary axis. At input powers used, the main regularities of the light distribution did not change. The pressure growth caused both the shift of intensity maximums towards electrodes and the decrease of the bright regions width. According to [Raizer, 1991] the intensive parts of the light distribution of the discharge belong to negative glow regions.

In the case of electrode configuration E2 the intensity distribution of singlet ($\lambda = 728.1$ nm) and triplet ($\lambda = 706.6$ nm) He spectral lines along the capillary axis were recorded by shifting the fibre. The distance between fibre tip and capillary wall was 2 mm. The intensity distribution shown in figure 15 was calculated considering the numerical aperture of the fibre. There was no difference between the distributions of $\lambda = 706.6$ nm and $\lambda = 728.1$ nm lines. In the main part between the electrodes the intensity was almost independent of

coordinate z and only very close to the electrodes a considerable growth of intensity took place. The variation of the N_2 fraction as well as the input power did not change the distribution between electrodes; however, the increase of the input power caused the expansion of the discharge out of the inter-electrode space.

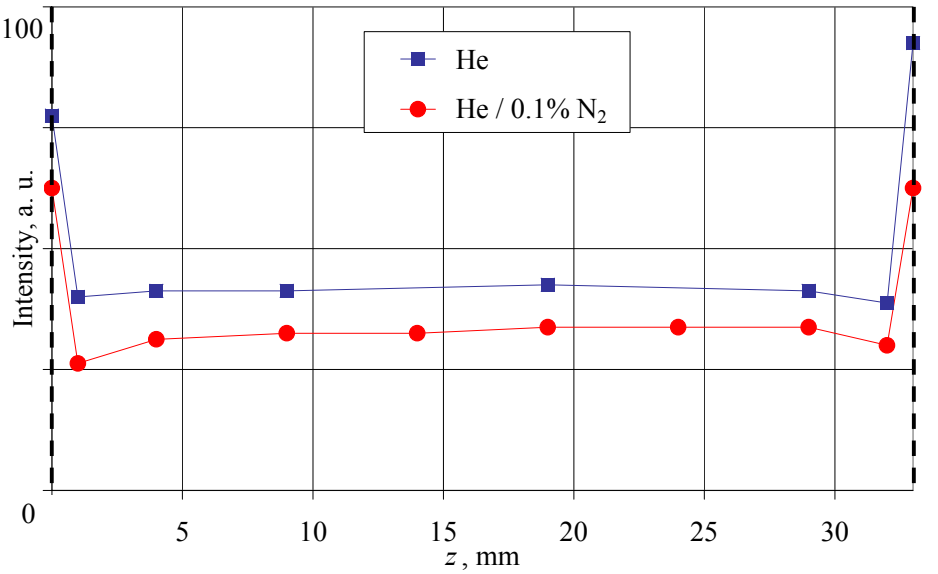

Figure 15. Intensity distribution along the capillary axis. Current i = 0.1 A, p = 60 Torr, λ = 706.5 nm. Vertical dashed lines mark the edges of electrodes. Electrode configuration E2.

4.2. Discharge mode

In the case of electrode configuration E1, the main experiments were carried out at the product of pressure, p, and discharge gap length, L, $p \cdot L$ = 12 Torr cm while in the case of configuration E2, $p \cdot L$ = 204 Torr cm. According to [Raizer, 1991], if in He $p \cdot L < (p \cdot L)_{CR}$ = 150 Torr cm, the discharge could run both in α and γ-mode. At higher $p \cdot L$ values only the γ-mode of discharge is possible. Thus in the case of configuration E1 both modes are achievable while in the case of E2 only the γ-mode of discharge is possible. However, there are a number of arguments indicating that the discharge in the case of E1 ran also in the γ-mode. Firstly, according to figure 14 the intensity distribution depended strongly on the pressure. This effect is characteristic to the γ-mode of discharge [Hasilev, 1980]. Secondly, in our experiments with quartz capillary tube an intensive sputtering of material was found. This effect indicates the significance of ion bombardment of capillary walls. According to [Raizer, 1991]

ion bombardment is in the α-mode discharge negligible. Lastly, the intensity of the λ = 706.5 nm line exceeded the intensity of N_2 (B-A) bands by an order of magnitude (figure 29). This effect is characteristic to the discharge to the discharge in γ-mode [Yang, 2004]. These findings confirms that the discharge of configuration E1 is also the γ-mode one.

4.2. Electrical characteristics

4.2.1. *i-u* curves

Figure 16 shows *i-u* curves recorded in the case of electrode configuration E1 for vacuum and discharge at different N_2 fractions.

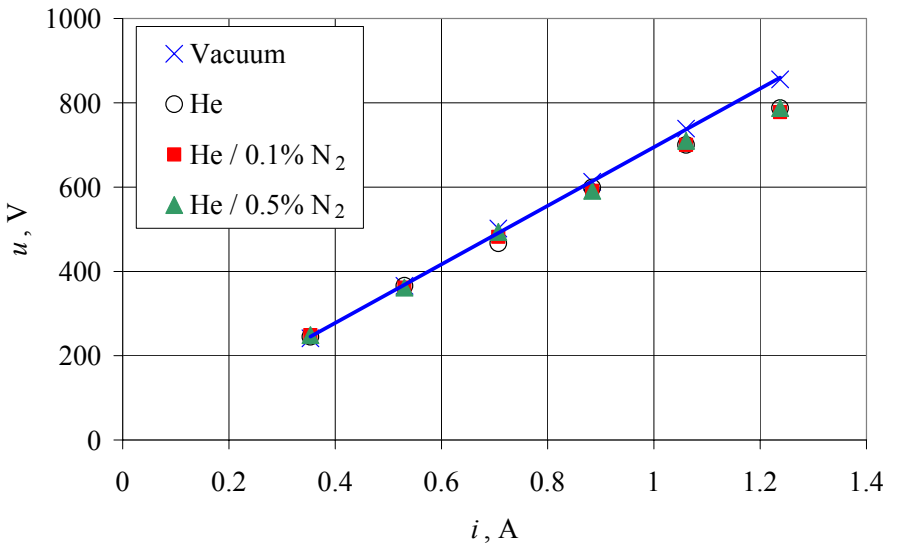

Figure 16. *i-u* curves in the case of electrode configuration E1. Best fit by the linear law is shown for vacuum by solid line; p = 60 Torr.

In the case of the evacuated capillary tube, i was a linear function of u while in the case of discharge *i-u* curves became sub-linear. The variation of the nitrogen concentration (0.01 - 0.5 %) did not cause remarkable changes in the shape of *i-u* curve.

Figure 17 shows *i-u* curves recorded in the case of electrode configuration E2 for vacuum and discharge at different N_2 fractions.

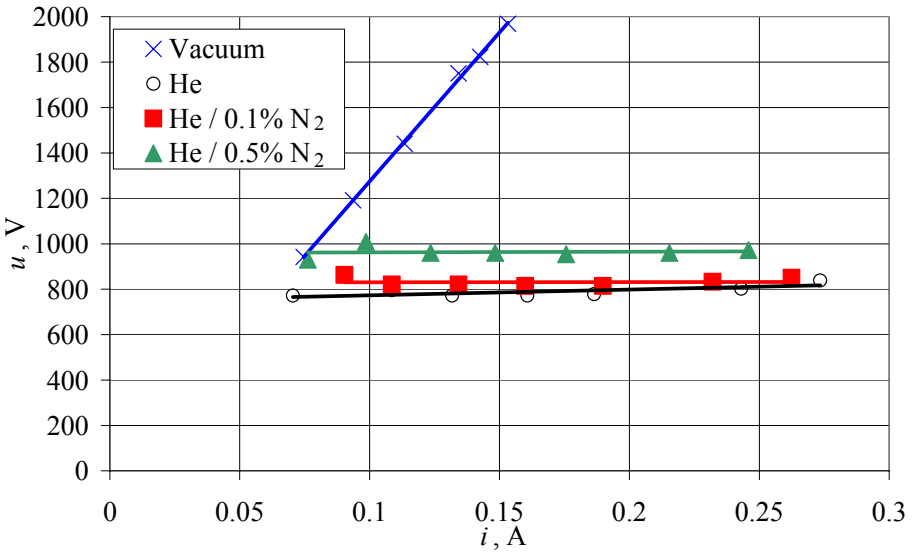

Figure 17. *i-u* curves in the case of electrode configuration E2. Best fits by the linear law are shown by solid lines; p = 60 Torr.

Differently from *i-u* curves recorded in the case of electrode configuration E1, voltage practically did not depend on current. Increase of N_2 fraction caused a parallel shift of *i-u* curve toward to the higher voltages.

4.2.2. Phase shift between current and voltage in the plasma

The phase shift, φ between the current and voltage was determined from the analysis of Lissajous figures. Examples, recorded in the case of electrode configuration E2 are presented in figure 18. Lissajous figures were recorded with digital oscilloscope Velleman PC5500. Without the discharge, the circuit is purely capacitive, i.e. φ should be 90°. Actually, in the case of evacuated tube there was a phase shift, φ_V, different from 90° which was caused by different length of cables. Phase shift in the plasma was calculated as $\varphi_{PL} = 90^\circ - (\varphi_V - \varphi_D)$ where φ_D is the phase shift measured in the case of discharge. Plasma phase shifts were determined for various current values and N_2 fractions.

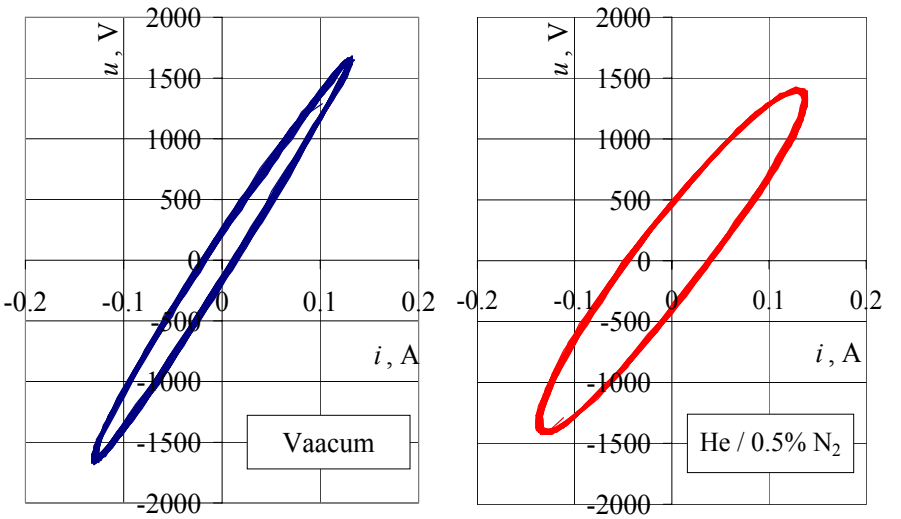

Figure 18. Example of Lissajous figures recorded in the case of electrode configuration E2 for vacuum and the gas discharge; He / 0.5% N_2; p = 60 Torr.

In the case of electrode configuration E1, at N_2 fractions < 0.1% the phase shift was almost constant, $\varphi_{PL} = 88.2^{\circ}$. At the highest fraction of N_2, 0.5%, the phase shift was $\varphi_{PL} = 86.9^{\circ}$.

When the electrode configuration E2 was used, the dependence of φ_{PL} on N_2 fraction was not detectable. The current growth from 0.06 to 0.27 A caused the phase shift decrease from 85º to 65º.

4.2.3. Plasma current and voltage on the plasma

Equivalent circuits (figure 19) based on the γ-mode discharge model [Raizer, 1996], were used to determine plasma voltage, u_{PL}, and current, i_{PL}, at different external conditions (current, voltage on the electrodes, N_2 concentration). Circuits consist from following capacitors:
C_s – stray capacitance – capacitance of connecting wires etc.;
C_w – capacitance of the capillary wall;
C_G – capacitance of the gas gap.
The complex resistance, Z_{PL}, consists from two capacitors equivalent to near-electrode sheets and plasma resistance connected in series with capacitors.

Two equivalent circuits, presented in figure 19, characterize real circuits at two electrode configuration, E1 and E2. In the case of electrode configuration E2 the distance between electrodes was large and the capacitor C_G became irrelevant.

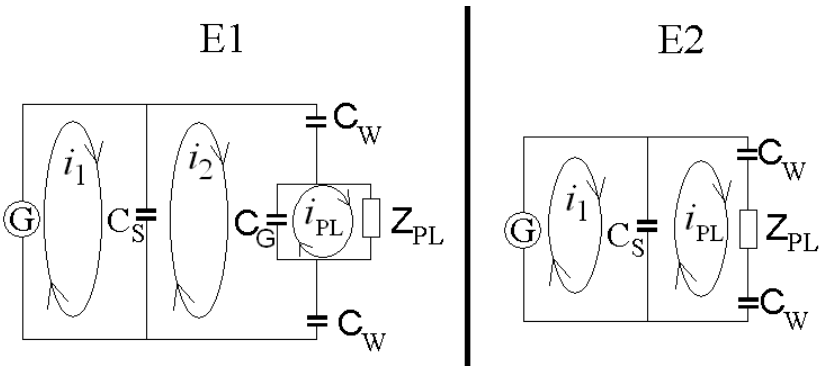

Figure 19. Equivalent circuit. G – generator, C_s – stray capacitance; C_w – capacitance of the capillary wall; C_G – capacitance of the gap; Z_{PL}– complex resistance of plasma.

For determining i_{PL}, u_{PL}, the set of Kirchhoff's equations was solved. The direction of currents in figure 19 is marked by arrows. In the case of electrode configuration E1, set of equations could be written as

$$\begin{cases} i_1 \cdot \dfrac{1}{j \cdot \omega \cdot C_s} - i_2 \cdot \dfrac{1}{j \cdot \omega \cdot C_s} = u \\ -i_1 \cdot \dfrac{1}{j \cdot \omega \cdot C_s} + i_2 \left(\dfrac{1}{j \cdot \omega \cdot C_s} + \dfrac{2}{j \cdot \omega \cdot C_w} + \dfrac{1}{j \cdot \omega \cdot C_G} \right) - i_{PL} \cdot \dfrac{1}{j \cdot \omega \cdot C_G} = 0 \\ -i_2 \cdot \dfrac{1}{j \cdot \omega \cdot C_G} + i_{PL} \left(Z_{PL} + \dfrac{1}{j \cdot \omega \cdot C_G} \right) = 0 \end{cases}$$

For electrode configuration E2 the set of equations is

$$\begin{cases} i_1 \cdot \dfrac{1}{j \cdot \omega \cdot C_s} - i_{PL} \cdot \dfrac{1}{j \cdot \omega \cdot C_s} = u \\ -i_1 \cdot \dfrac{1}{j \cdot \omega \cdot C_s} + i_{PL} \left(\dfrac{1}{j \cdot \omega \cdot C_s} + \dfrac{2}{j \cdot \omega \cdot C_w} + Z_{PL} \right) = 0 \end{cases}$$

Here ω – angular frequency, $i_1 = i \cdot \exp(j \cdot \varphi)$; i, u and φ are measured values known from experiment.

The set of equations was solved using MathCad 2001i software. Values of capacitance were determined as follows. The total capacitance of the circuit, C_T, was determined on the basis of i–u characteristic recorded in the case of the evacuated capillary tube, figure 16, 17. For electrode configuration E1, C_T = 7.8 pF, for E2, C_T = 0.45 pF. The capacitance of the capillary wall, C_W, for

E1 was calculated using the formula for plate capacitor with surface area of electrode and with interelectrode distance equal to the capillary wall thickness; $C_W = 52$ pF. For E2 the formula of a cylindrical capacitor was used; $C_W = 10$ pF. For ceramic permittivity the value 9.2 [Reiche, 1994] was used. The capacitance of the gas gap for E1, $C_G = 2.5$ pF, was calculated using the formula for plate capacitor with interelectrode distance equal to capillary inner diameter. Known values of C_W, C_G and C_T allowed to calculate the stray capacitance. For E1, $C_S = 5.6$ pF, for E2 $C_S = C_T = 0.45$ pF.

Calculated $u_{PL} = f(i_{PL})$ are shown in figure 20 and 21.

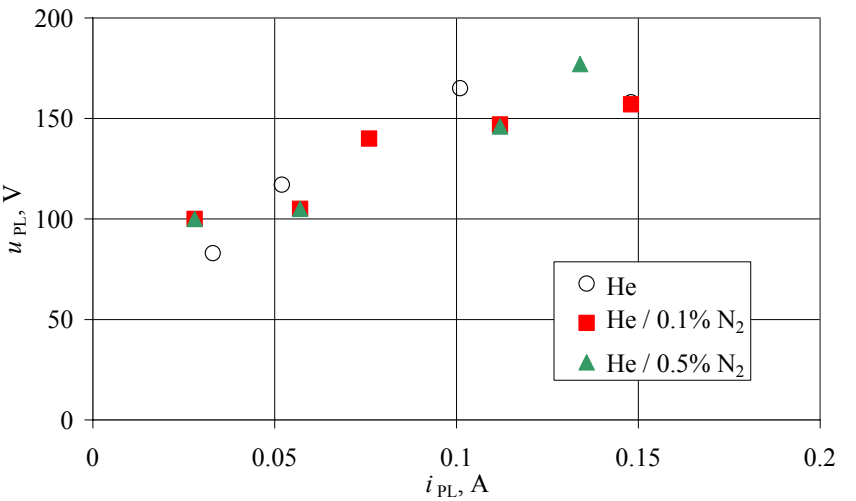

Figure 20. Voltage on the plasma, u_{PL} as a function of the plasma current, i_{PL}; $p = 60$ Torr. Electrode configuration E1.

According to figure 20 u_{PL} increases with the growth of i_{PL}. Addition of N_2 did not change the i_{PL}-u_{PL} curve.

Figure 21 shows that in the case of electrode configuration E2 at a fixed fraction of N_2, the voltage u_{PL} is almost independent on i_{PL}, i.e. the plasma column between electrodes behaves like the normal glow discharge [Raizer, 1991]. When the N_2 fraction did not exceed 0.25%, within the experimental uncertainty the plasma voltage was the same, $u_{PL} \approx 500$ V. At 0.5% of N_2 fraction, the plasma voltage had higher value, $u_{PL} \approx 700$ V.

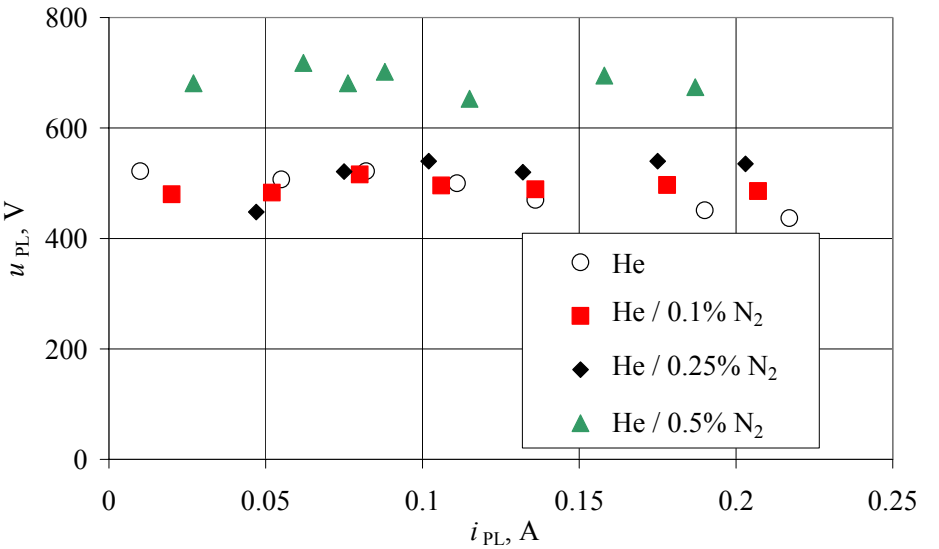

Figure 21. Voltage on the plasma, u_{PL} as a function of the plasma current, i_{PL}; p = 60 Torr. Electrode configuration E2.

4.2.4. Electron density

The electron density was calculated as $[e] = \frac{i_{PL}}{S_i \cdot \mu \cdot e \cdot E}$. Here e is the elementary charge, E – electric field strength and S_i – cross-section of the current. The value of electron mobility $\mu = 1.43 \cdot 10^4$ cm^2 V^{-1} s^{-1} was taken from [Raizer, 1991] and it was assumed that low N_2 fraction does not change the value of mobility.

Electric field strength in the negative glow region (electrode configuration E1) is very weak [Lawler 1991]. In calculations of electron density the field strength E = 2 V cm^{-1} was used (E/N = 0.1 Td). The cross-section of the current was taken equal to the area of the powered electrode, S_i =4.75 cm^2. At plasma currents used, (0.03 – 0.15 A), the electron density in the negative glow was in the range $1 \cdot 10^{12} - 7 \cdot 10^{12}$ cm^{-3}.

To determine field strength in the positive column (electrode configuration E2), *i-u* curves were recorded at different distances between powered and grounded electrodes, L. At a constant current the voltage grew linearly with the distance between electrodes, figure 22. The slope of the dependence $u = f(L)$ gave the value of the electric field strength, $E_{PC} \approx 110$ V/cm.

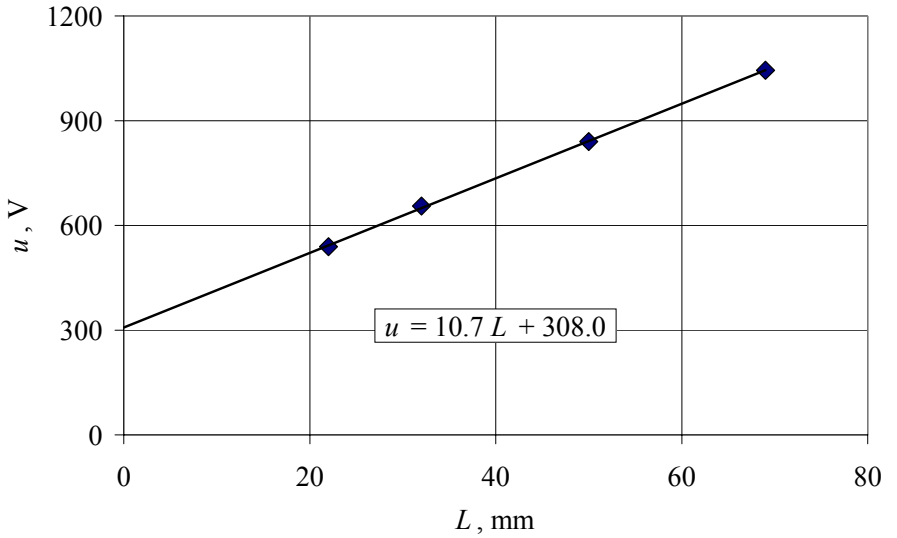

Figure 22. Voltage, u, as a function of distance between electrodes L; $i = 0.08$ A; He; $p = 60$ Torr. Best fit by linear law is shown by solid line.

The cross-section of the current, was taken equal to the inner cross-section of capillary, $S_i = 0.03$ cm^2. At used plasma currents (0.02 – 0.22 A) electron density in the positive column was in the range $3 \cdot 10^{12} - 3 \cdot 10^{13}$ cm^{-3}.

4.2.5. Electron energy distribution function (EEDF)

The excitation and ionization abilities of electrons are determined by EEDF. In the positive column, EEDF was found using the freeware code BOLSIG+ [available from www.siglo-kinema.com/bolsig.htm]. BOLSIG+ calculates also EEDF-related macroscopic parameters like mean energy, transport coefficients and rate coefficients.

Figure 23 gives EEDFs for pure He and He / 0.5% N_2 mixture corresponding to the field strengths in the positive column of our experiment (subsection 4.2.4). The mean energy of electrons in He was $T_e = 2.4$ eV and in He / 0.5% N_2, it was $T_e = 1.8$ eV. According to figure 23 main differences between EEDFs of He and He / N_2 mixture appear at electron energies $\varepsilon < 7$ eV and $\varepsilon > 15$ eV: addition of N_2 introduces extra loss channels of electron energy.

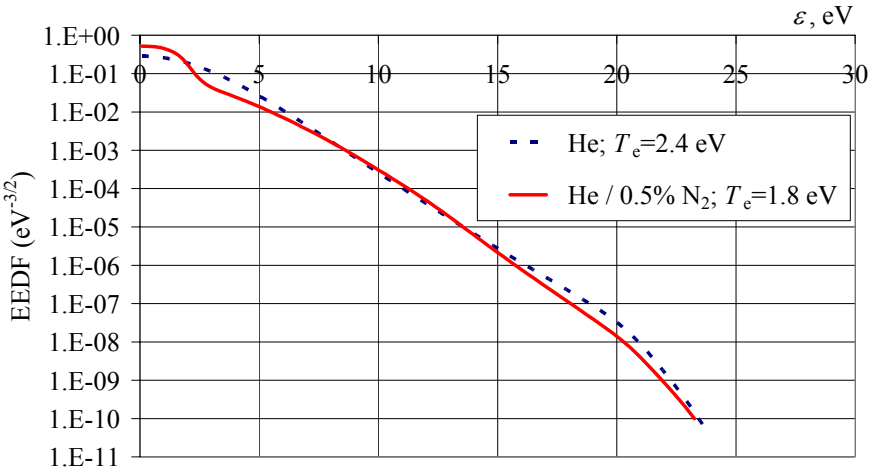

Figure 23. EEDF of He (E/N =6.0 Td) and He / 0.5% N_2 (E/N = 7.2 Td). T = 1100 K, ν = 27 MHz. Calculated using BOLSIG+ code.

Figure 24 characterizes electron energy loss in the positive column. In the inset of figure 24 are shown energy losses of electrons in elastic and inelastic collisions with He atoms and N_2 molecules as a function of N_2 fraction.

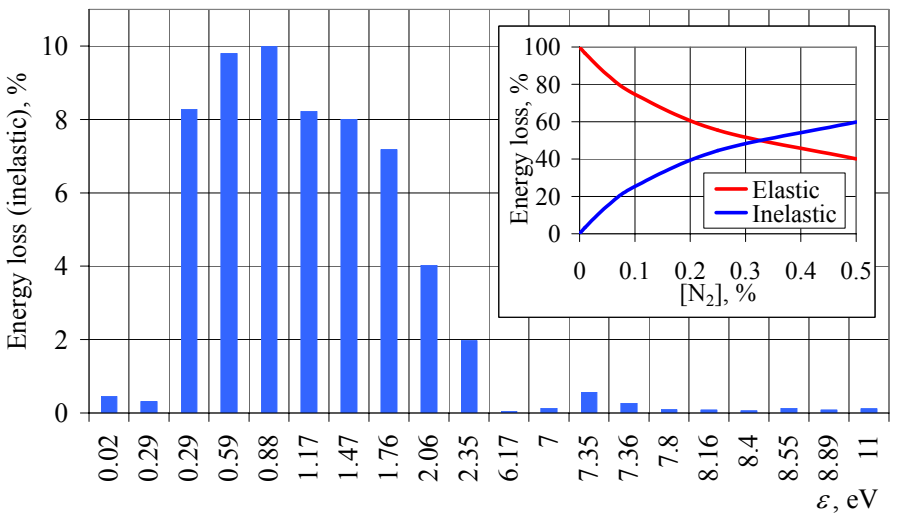

Figure 24. Electron energy loss fraction in inelastic collisions with N_2. He / 0.5% N_2; E/N = 7.2 Td; T = 1100 K; ν = 27 MHz. Inset: electron energy losses as a function of N_2 fraction. T = 1100 K; ν = 27 MHz. E/N increased with [N_2] growth gradually from 6.0 Td (He) up to 7.2 Td (He / 0.5% N_2). Calculated using BOLSIG+ code.

According to the inset of figure 24 at $[N_2] < 0.35\%$ elastic losses are dominant. Main contribution to the elastic energy losses gives electron collisions with He atom, for N_2 the highest elastic loss percentage was only $\approx$ 0.06% (mixture He / 0.5% N_2). At $[N_2] > 0.35\%$ inelastic losses become dominant. Nearly all inelastic energy losses are caused by collisions with N_2 molecule. According to figure 24 electrons lose their energy dominantly (≈ 58 %) in excitation of $N_2(X)$ vibrational states. Ca 1 % is lost in excitation of electronic B (threshold energy $E_{th} = 7.35$ eV) and W ($E_{th} = 7.36$ eV) states of N_2.

In the negative glow region, the EEDF calculated on the basis of BOLSIG+ does not characterise the excitation/ionization processes as the mean electron energy is low and the excitation/ionization is caused by non-equilibrium, fast electrons. Figure 25 presents EEDF calculated for two different *E/N* values and EEDF of the negative glow region determined experimentally [Soldatov, 1976]. The "body" of EEDF ($\varepsilon < 1$ eV), calculated for $E/N = 0.5$ Td does not differ much from the experimental one.

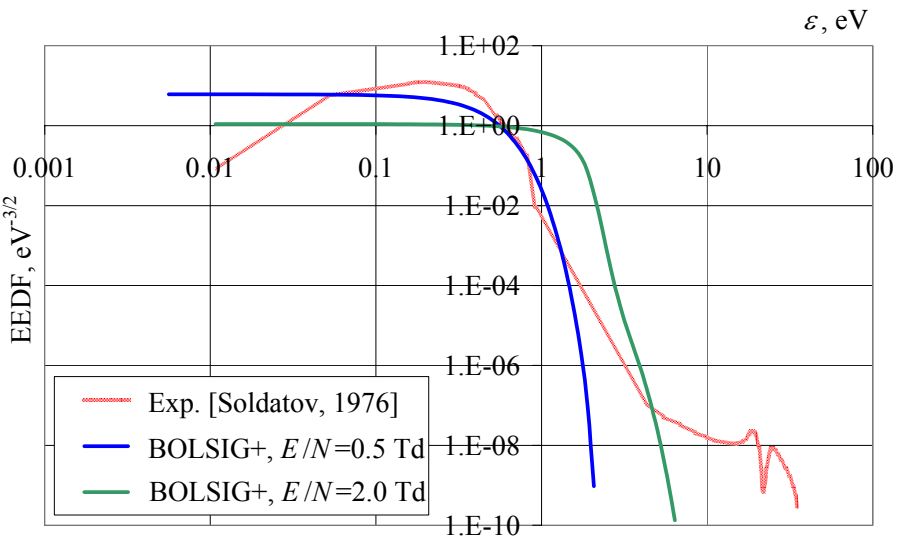

Figure 25. Experimental and calculated EEDFs of He / 3% N_2. Experimental EEDF [Soldatov, 1976]: hollow cathode discharge, total pressure $p = 3$ Torr. Calculated EEDFs: at *E/N* values 0.5 and 2.0 Td; $T = 500$ K.

4.3. Results of spectral measurements

The spectra of the discharge were recorded as a function of the plasma current, the total pressure and N_2 fraction.

4.3.1. Spectra of He discharge

In figure 26 is shown typical spectrum of He discharge recorded from the negative glow region (electrode configuration E1). In the spectral range λ = 200–800 nm the most intensive spectral line was of He at 706.5 nm. Some bands, which could belong to the radiation of He_2 molecule (near wavelengths 440, 462–473, 535, 573, 596, 640 nm), were very weak and they were not clearly distinguishable. Some bands and lines belonging to O, O_2^+, CO and H were presented in the spectrum. At the same time the band of OH near 308 nm, which is usually very easily excited in discharges, was missing. In the spectral region λ = 800–1200 nm, besides the strongest line of He at 1083.0 nm the lines of O, at 844.6 and 926.1 nm, were recorded, figure 27. The contribution of impurities in the spectrum increased with the growth of input power. Therefore their appearance may be connected with the sputtering of the material of capillary walls.

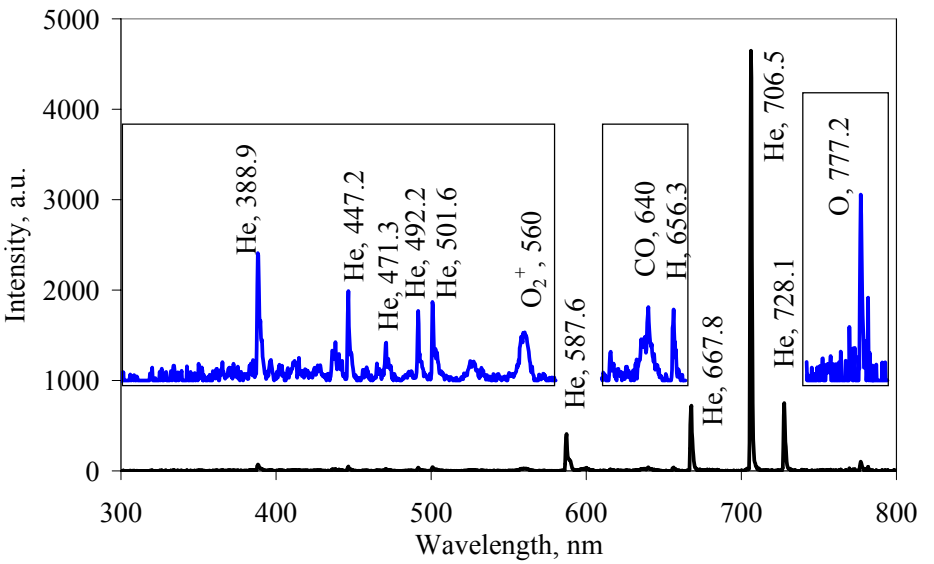

Figure 26. Spectrum of the negative glow (electrode configuration E1) in He; i_{PL} = 0.1 A; p = 60 Torr; axial direction. Insets: the intensity is multiplied by factor 25. Registered with USB2000 spectrometer.

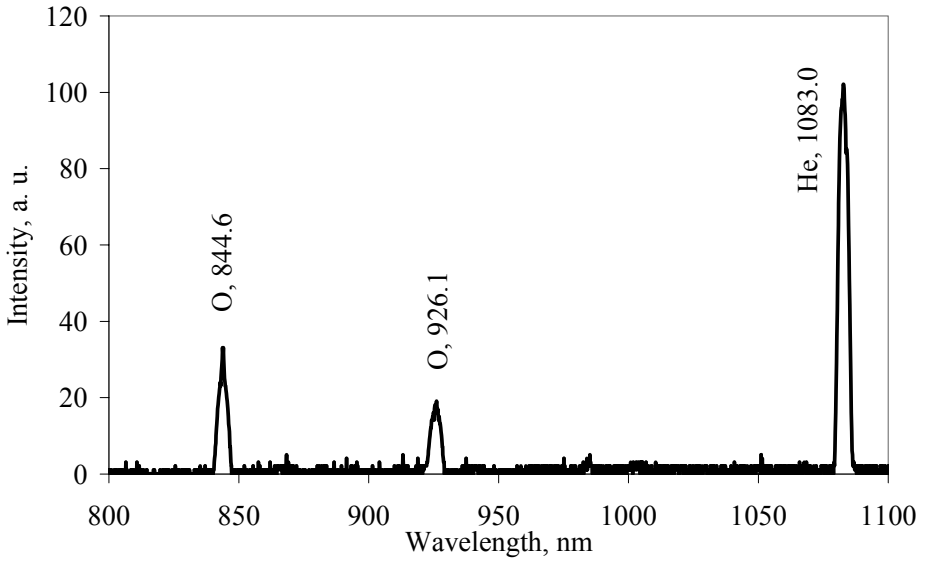

Figure 27. Spectrum of the negative glow (electrode configuration E1) in He; i_{PL} = 0.12 A; p = 60 Torr; axial direction. Registered with MDR-23 spectrometer.

In figure 28 is He discharge spectrum recorded from the positive column region (electrode configuration E2).

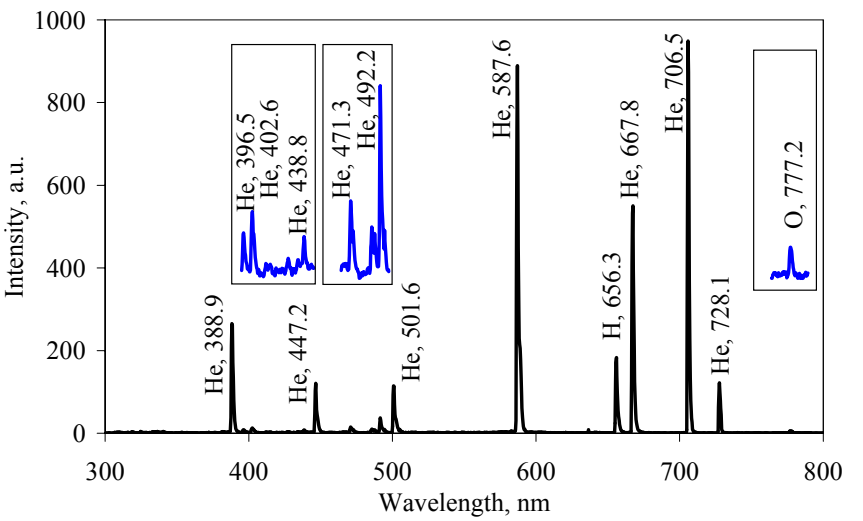

Figure 28. Spectrum of the positive column (electrode configuration E2) in He; i_{PL} = 0.06 A; p = 60 Torr; axial direction. Insets: the intensity is multiplied by factor 20. Registered with USB2000 spectrometer.

The most intensive line in the spectrum was He λ=706.5 nm line. Comparing this spectrum with that registered in the negative glow (figure 26), one can see that the contribution of He spectral lines at wavelengths 388.9, 447.2, 587.6 nm grows significantly, and spectral lines at 402.6, 438.8 nm which arise due to transitions from high laying energy state (He(5^1S), E=24.04 eV), are detectable. The impurity bands and lines were the same as in the case of negative glow (figure 26). However, bands of O_2^+ (560 nm) and CO (640 nm) intensity of which in spectrum of negative glow was relative high, in the positive column were almost missing. At the same time intensity of H line at 656.3 nm was considerably higher.

4.3.2. Spectra of He / N_2 discharge

In figure 29 is the spectrum of He / 0.01% N_2 mixture discharge recorded from the negative glow region. The addition of a small amount of N_2 causes the appearance of numerous bands belonging to N_2 and its ion. The bandhead intensity of N^+_2 (B–X, 0–0) transition at 391.4 nm was comparable to the intensity of the most intensive line of He at 706.5 nm. The bands of neutral N_2 belonging both to C–B (most intensive bandheads at 337, 357 nm) and B-A (most intensive bandheads at 750, 775 nm) electronic transitions were less intensive. Spectral lines belonging to impurities were not detectable; for example the band of O_2^+ at 560 nm presented in the spectrum of "pure" He discharge was now missing.

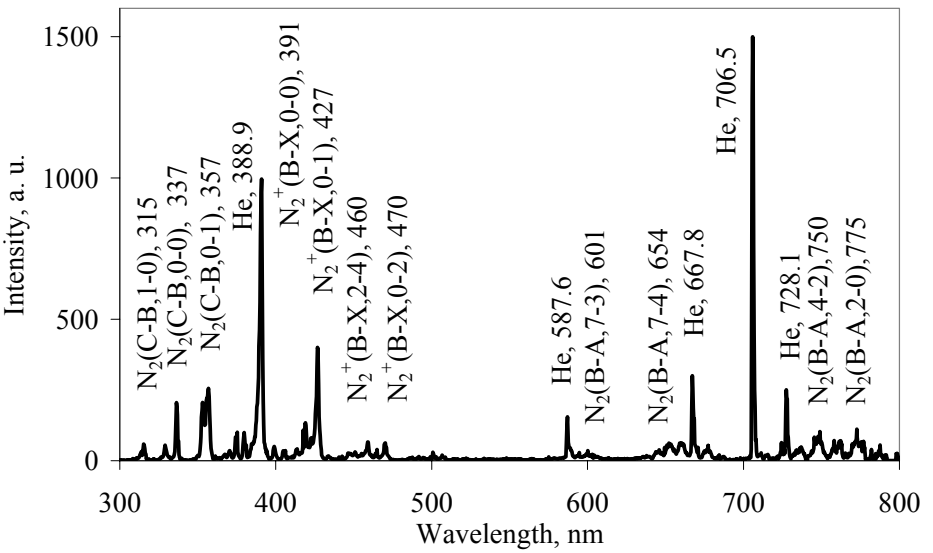

Figure 29. Spectrum of negative glow (electrode configuration E1) in He / 0.01% N_2; i_{PL} = 0.1 A; p = 60 Torr; axial direction. Registered with USB2000 spectrometer.

In figure 30 is the spectrum of He/0.01% N_2 discharge recorded from the positive column region.

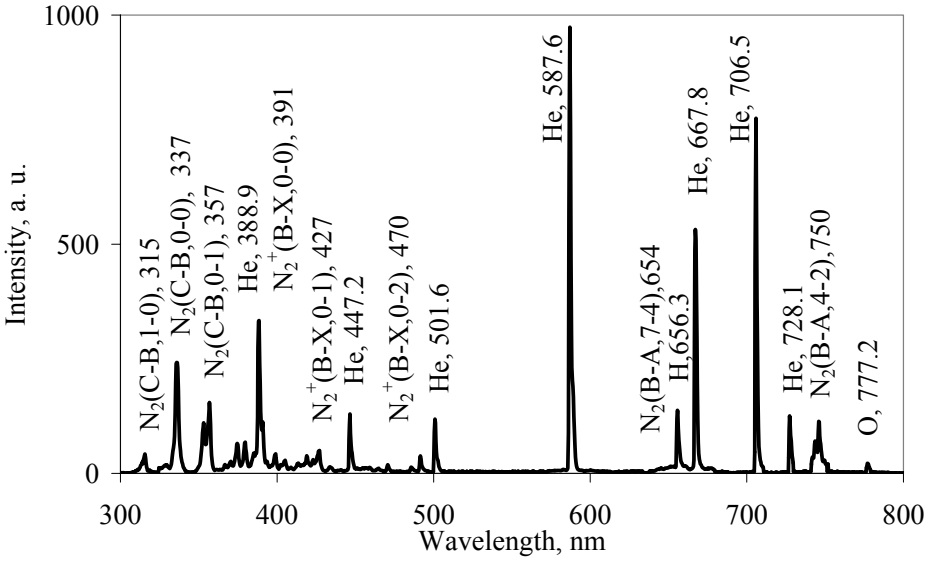

Figure 30. Spectrum of positive column (electrode configuration E2) in He / 0.01% N_2; i_{PL} = 0.06 A; p = 60 Torr; axial direction. Registered with USB2000 spectrometer.

The most intensive in the spectral range 300–800 nm was He line at 587.6 nm. Intensive bands of neutral N_2 belonged to the second positive system (C-B electronic transition, bandheads at 337, 357 nm); the bands of the first positive system (B–A transition) are less intensive. Among N_2^+ bands the most intensive one belong to the transition (B–X, 0–0), bandhead at 391.4 nm. Among the impurity lines the most intensive are lines of H (656.3 nm) and O (777.2 nm).

4.3.3. Gas temperature

The gas temperature was estimated on the base of N_2^+(B) rotational temperature. This method basis on the assumption that the the rotational temperature of N_2^+ ions and the translational temperature are equal. In the low pressure ($p \approx 1$ Torr) afterglow study [Endoh, 1983] it was found that in He / N_2 mixture discharge the rotational temperature of N_2^+(B) depends strongly on N_2^+ production mechanism: in the case of Penning ionization, the initial rotational temperature is close to the ambient gas temperature while in the case of charge transfer reaction it exceeds the gas temperature more than 500°C. Therefore the rotational temperature is interpretable as the gas temperature only if N_2^+(B) rotational relaxation time to thermal equilibrium is shorter than the lifetime of

the state. According to the simulation [Bibinov, 2001], in the atmospheric pressure He / N_2 discharge the rotational relaxation of $N_2^+(B)$ from the initial temperature of 1000 K to the gas temperature of 500 K lasts $\tau_{RX} \approx 5$ ns. As in our experiment the pressure was ca 10 times lower, the relaxation to the thermal equilibrium lasts approximately 10 times longer, i.e. $\tau_{RX} \approx 50$ ns. The effective lifetime of $N_2^+(B)$, τ_{LT}, depends on the radiative lifetime of the state as well as on the three-body quenching, $\tau_{LT} = \dfrac{1}{A_{391} + k_{KN1} \cdot [He] \cdot [N_2] + k_{KN2} \cdot [N_2]^2}$

Here $A_{391} = 1.214 \cdot 10^7\ s^{-1}$- probability of radiative transition N^+_2 (B–X, 0–0) at $\lambda \approx 391$ nm [Laux, 1992]; k_{KN1} and k_{KN2} are rate coefficients of N_2^+ conversion reactions (see subsection 4.4.1). The shortest effective lifetime is for the N_2 concentration, 0.5%: $\tau_{LT} \approx 80$ ns. Consequently, as $\tau_{LT} > \tau_{RX}$, the rotational temperature of $N_2^+(B)$ should be close to the gas temperature.

For the determination of the rotational temperature, T_R, the convolution integral of the apparatus function and the rotational spectrum was calculated. The apparatus function was determined experimentally using a HeNe laser and the data needed for calculation of the rotational spectrum were taken from [Naghizadeh-Kashani, 2002]. The temperature was determined fitting the calculated spectrum with the experimentally recorded one. In figure 31 is shown an example of measured and calculated spectra.

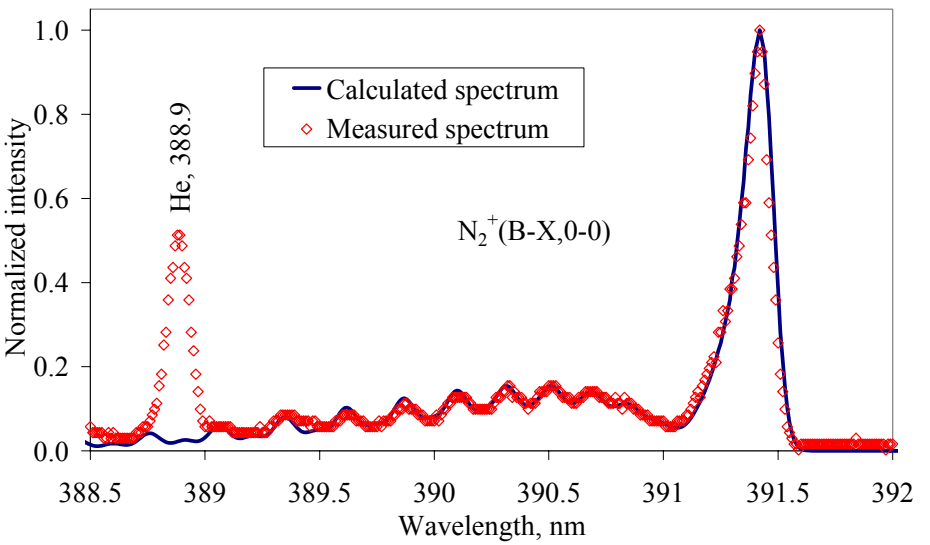

Figure 31. Example of $N_2^+(B–X, 0–0)$ spectrum. Calculated spectrum corresponds to the temperature T_R = 550 ± 100 K. Measured spectrum: negative glow region (electrode configuration E1), He / 0.01% N_2; i_{PL} = 0.14 A; p = 60 Torr; axial direction. Registered with GCA/McPherson EU/E-700 spectrometer.

In the case of electrode configuration E1 the growth of plasma current (from 0.02 to 0.17 A) caused linear increase of temperature from 300 to 600 K. In the case of electrode configuration E2 the temperature, 1100 K, did not depend on the current through the plasma. The independence of temperature on the discharge current could be explained by efficient cooling and/or the expansion of the discharge volume with the current growth.

4.3.4. Density of atoms in the metastable state, He(2^3S)

The density of metastable state atoms was estimated using data of He spectral line intensities recorded from the lateral, I_L, and axial, I_A, directions. For the most of He lines, the ratio $R = I_L / I_A$ did not depend on N_2 concentration, $[N_2]$. An exception was He λ = 1083.0 nm line: for this line the ratio decreased with the growth of $[N_2]$. Example of ratio $R(\lambda = 1083.0$ nm) as a function of $[N_2]$, is presented in figure 32. As 1083.0 nm spectral line arises from transition where the lower state, He(2^3S), is a metastable one, this effect should be caused by self-absorption. Decrease of $R(\lambda = 1083.0$ nm) is explicable with quenching of He(2^3S) by N_2 in the Penning reaction (2.25). According to our set up (subsection 3.5), geometrical factors in the lateral and the axial directions were equal. Thus, neglecting the absorption in the lateral direction, the ratio could be written as $R = \frac{D \cdot \kappa}{1 - e^{-\kappa \cdot L}}$, [Frish, 1970]. Here D is the inner diameter of the capillary, κ is the absorption coefficient and L is the length of the discharge along capillary axis. On the other hand the density of metastable atoms He(2^3S) could be expressed as $\left[\mathrm{He}(2^3\mathrm{S})\right] = \frac{4 \cdot \pi \cdot c \cdot \kappa}{\sqrt{\frac{\ln 2}{\pi}}} \cdot \frac{g_i}{g_k} \cdot \frac{\Delta\lambda_D}{\lambda_{ki}^4 \cdot A_{ki}}$.

Here c denotes the speed of light, $\lambda_{ki} = 1083.0$ nm; $g_i = 3$, $g_k = 9$ are statistical weights of He(2^3S) and He(2^3P) states, respectively, and $A_{ki} = 10^7$ s^{-1} is the probability of radiative transition He(2^3P–2^3S) [Weise. 1969]. Combining the last two equations and using the experimentally determined ratio R, the density of He metastable atoms was calculated. The contour of the spectral line was taken as the Doppler one. In the case of negative glow the contour width, $\Delta\lambda_D = 0.0087$ nm was calculated for the temperature $T = 500$ K, for the positive column region $\Delta\lambda_D = 0.013$ nm ($T = 1100$ K).

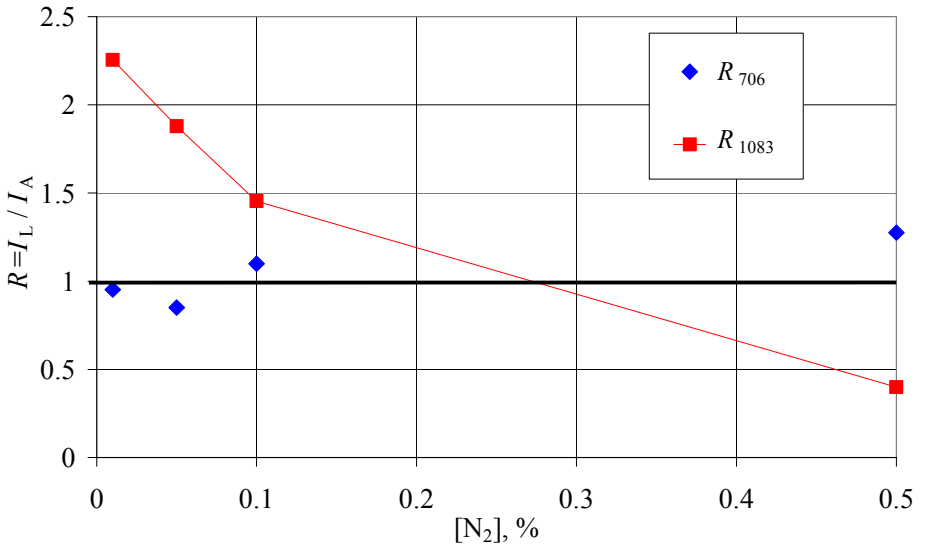

Figure 32. Ratio of He lines intensities (706.5 and 1083.0 nm), registered from the lateral and axial directions as a function of $[N_2]$. Negative glow region (electrode configuration E1), i_{PL} = 0.1 A; p = 60 Torr.

In figure 33 is shown $[He(2^3S)]$ as a function of $[N_2]$.

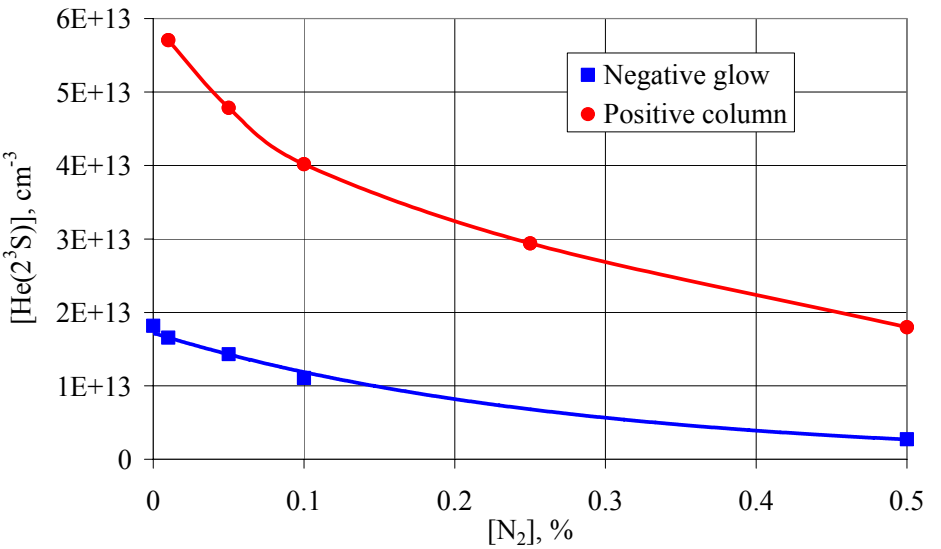

Figure 33. Calculated densities $[He(2^3S)]$ in the negative glow (electrode configuration E1) and positive column (electrode configuration E2) as a function of $[N_2]$; $[e] \approx 7 \cdot 10^{12}$ cm^{-3}, p = 60 Torr.

4.4. Excitation and ionization mechanisms in He / N_2 mixture discharge

Many important parameters of plasma like frequencies of quenching of excited states by He, He_2^+ production in conversion reaction, vibrational de-excitation of He_2^+ by He atoms etc depend on gas density. Therefore the main conclusions about the excitation and ionization mechanisms of helium and nitrogen are drawn on the base of dependence $I_\lambda = f([N_2])$ recorded at $p = 60$ Torr and at a fixed value of the electron density. Other dependences like $I_\lambda = f(i_{PL})$, $I_\lambda = f(p)$ have a supporting character.

4.4.1. Nitrogen ion production mechanisms

In figure 34 is shown a schematic diagram of the production and loss mechanisms of the molecular ions of nitrogen and corresponding rate coefficients used in following discussion.

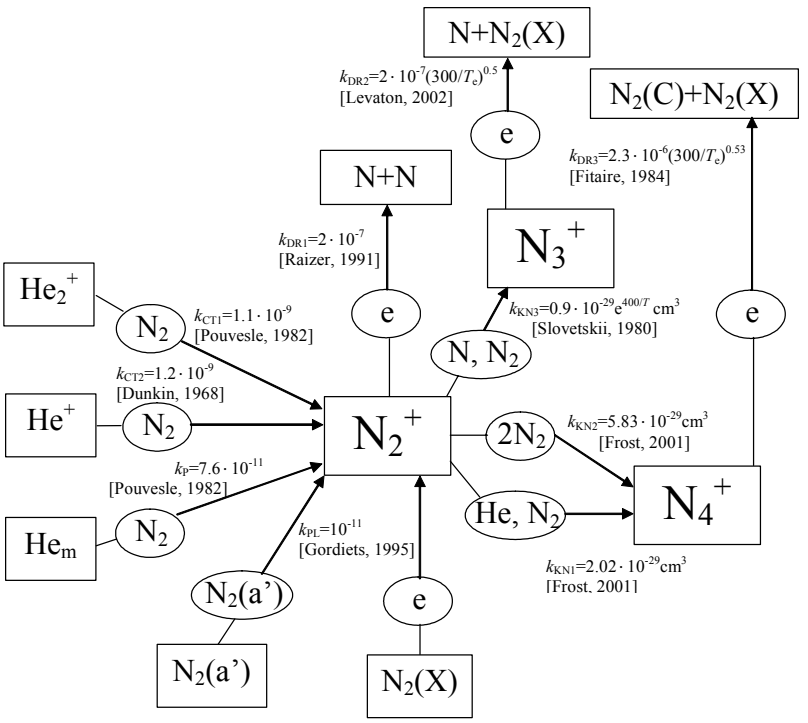

Figure 34. Schematic diagram of nitrogen ion production and loss mechanisms in He / N_2 mixture. Rates are in cm^3s^{-1}, temperature (T_e, T) in Kelvin. Rate coefficients: k_{PL}– Pooling reaction, k_P – Penning reaction, k_{CT1}, k_{CT2} – charge transfer reactions, k_{Dr1}, k_{DR2}, k_{DR3} – dissociative recombination reactions, k_{KN1}, k_{KN2}, k_{KN3} – conversion reactions.

According to literature overview (subsection 2.3) in He / N_2 mixtures four N_2^+ production mechanisms are considered: Penning reaction via He metastable state atoms, charge transfer reactions via He^+ and He_2^+, ionization of N_2 by electron impact and reaction between N_2 excited state molecules. In our conditions latter two mechanisms have a negligible role. Indeed, according to [Paris, 2004] in the case of ionization by electron impact (reduced electric field value $E/N < 500$ Td), the intensity of band N_2(C-B,0-0) ($\lambda = 337$ nm) exceeds that of N_2^+(B-X,0-0) ($\lambda = 391$ nm) more than an order of magnitude. Contrary, our experiments in the negative glow region showed that the intensity of band at $\lambda = 391$ nm exceeds that of $\lambda = 337$ nm ca three times (figure 29). However, in the positive column region these bands have almost the same intensities. The knowledge of the field strength in this region (subsection 4.2.4.) allowed to calculate the rate of the direct ionization, R_{direct}. Using the BOLSIG+ code it was found the rate coefficients for different N_2 concentrations. The highest rate of electron impact ionization, $R_{direct} \sim 10^{14}$ cm^{-3} s^{-1} was found for [N_2] = 0.1% (rate coefficient, $k_{0.1\%N2} = 3.5 \cdot 10^{-15}$ cm^3 s^{-1}). This is ca four orders of magnitude smaller than that of Penning reaction (figure 38). The experimental finding that N_2^+ (B–X) bandhead intensity does not depend on the current (figure 35) allows to reject the other electron-related mechanisms like the stepwise ionization from N_2 excited states.

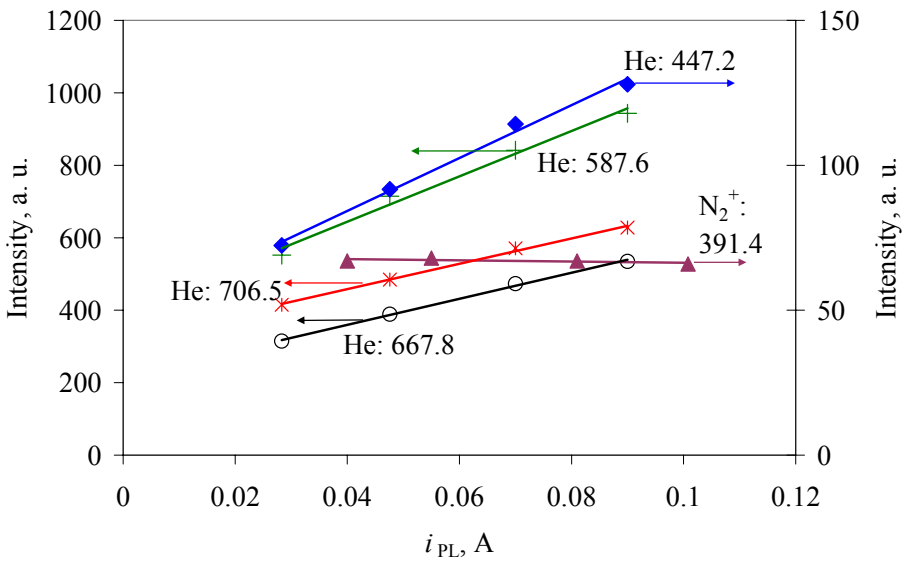

Figure 35. Intensities of N_2^+ (B–X) bandhead ($\lambda = 391.4$ nm) and He lines as a function of plasma current; positive column region; He / 0.25% N_2 mixture; $p = 60$ Torr; axial direction. Points- experiment; best fits by linear law are shown by solid lines.

In our conditions the ionization via reactions between N_2 excited state molecules could be also reject. According to [Levaton, 2002] the highest rate of that kind of reactions has the pooling reaction with two N_2(a') molecules as

reactants. At our densities of He(2^3S) this reaction has a comparable rate to the Penning reaction only if more than 1% of all N_2 species are in the N_2(a') state. Such a high concentration of N_2(a') is highly unreal.

Consequently both in positive column and negative glow regions at our conditions N_2^+ ions are produced mainly by Penning and/or charge transfer reactions. As at the pressure p = 60 Torr He^+ ions are very quickly converted to the He_2^+ ions (rate coefficient k_{konv}=1.1·10^{-31} cm^{6}s^{-1} [Smirnov, 1974]), the charge transfer reaction runs mostly via He_2^+ ions.

4.4.2. Nitrogen ion loss mechanisms

The main loss mechanisms of nitrogen ions are volume recombination and diffusion to the capillary walls. According to the previous subsection nitrogen ions are primary formed as N_2^+. Due to the conversion reactions (figure 34) these ions are partly converted to the complex ions N_3^+ and N_4^+. At low electron temperatures the recombination rate coefficient of N_4^+ is ca an order of magnitude larger than that of N_2^+. Therefore in some studies ([Märk, 1971], [Petrov, 2000]) the recombination of complex ions N_3^+ and N_4^+ are also considered. However, in our conditions the loss of nitrogen ions via N_4^+ recombination is negligible. Indeed, assuming that N_4^+ is mainly produced in conversion reactions (figure 34) the maximal ratio of N_4^+ production and N_2^+ recombination rates is $\frac{R_{\text{prod}}\left(N_4^+\right)}{R_{\text{rec}}(N_2^+)} = \frac{k_{\text{KN1}}\cdot[\text{He}]\cdot[N_2]+k_{\text{KN2}}\cdot[N_2]^2}{k_{\text{DR1}}\cdot[\text{e}]} \approx 0.3$. Thus, even if all ions N_4^+ recombine, the recombination rate of N_4^+ constitutes only ca 30% of that of N_2^+. The recombination rate coefficient of N_3^+, k_{DR2}, is close to that of N_2^+ but apparently N_3^+ density is much lower and thus this loss is also unimportant.

The frequency of N_2^+ diffusion loss, $\nu_{\text{Dif}}(N_2^+) = \frac{D}{\Lambda^2}$, was calculated according to formulas and data given in [Raizer, 1991]. Ambipolar diffusion coefficient, D, and diffusion length, Λ, can be expressed as

$$D \approx T_e \cdot \mu_i = T_e \cdot \left(\frac{2.7\cdot 10^4 \sqrt{1+\frac{M_{\text{He}}}{M_{\text{N2}}}}}{\sqrt{\left(\frac{\alpha}{a_0^3}\right)\cdot M_{\text{He}}}\cdot p} \right), \quad \Lambda = \left[\left(\frac{2.4}{r}\right)^2 + \left(\frac{\pi}{L}\right) \right]^{-\frac{1}{2}}$$

Here μ_i – mobility of N_2^+ in He, M_{He}, M_{N2} are molecular weights of He and N_2 correspondingly, α – polarizability, a_0 – Bohr radius (for He (α/a_0^3) = 1.39), r - capillary inside radius. For the electron temperature, T_e = 1 eV, which is

characteristic to the positive column, $\nu_{\mathrm{Dif}}(N_2^+) = 1.2 \cdot 10^5$ s^{-1} is much lower than the recombination frequency of N_2^+, $\nu_{\mathrm{rec}}(N_2^+) = 1.4 \cdot 10^6$ s^{-1}. In the case of negative glow T_e is lower, hence $\nu_{\mathrm{Dif}}(N_2^+)$ is still smaller.
Consequently, both in positive column and negative glow regions the main nitrogen ion loss mechanism is N_2^+ recombination.

4.4.3. N_2^+ and He_2^+ concentration, mechanisms of He_2^+ production

The densities of $[He_2^+]$ and $[N_2^+]$ were estimated on the base of quasineutrality condition and balance of nitrogen ion production and loss in the stationary discharge. Additionally it was taken into account that besides N_2^+ and He_2^+ in the discharge also other ions exist.

Considering production and loss mechanisms of nitrogen ions given in subsections 4.4.1 and 4.4.2, in the stationary case the production and losses of ions are balanced:

$$[N_2] \cdot (k_{\mathrm{CT1}} \cdot [He_2^+] + k_{\mathrm{P}} \cdot [He_m]) = k_{\mathrm{DR1}} \cdot [N_2^+] \cdot [e]$$

On the other hand in the positive column as well as in the negative glow regions the condition of quasineutrality is valid:

$$[e] = [He_2^+] + [N_2^+] + [M^+].$$

Here $[M^+]$ denotes the density of other ions.
The third relationship needed for the determination of unknown densities $[He_2^+]$, $[N_2^+]$ and $[M^+]$ is based on the assumption that N_2^+ (B), $v = 0$ state is populated by the same mechanisms as other N_2^+ states and depopulated because of radiation and charge conversion. Thus for the N_2^+(B) state population is valid the proportionality:

$$[N_2^+(B)] \propto \frac{[N_2^+]}{A_{391} + k_{\mathrm{KN1}} \cdot [N_2] \cdot [He] + k_{\mathrm{KN2}} \cdot [N_2]^2}$$

Densities $[He_2^+]$ and $[N_2^+]$ were calculated using $[M^+]$ as a free parameter. The value of $[M^+]$ was determined fitting the calculated relative value of $[N_2^+(B)]$ with the measured intensity at $\lambda = 391.4$ nm, figure 36.

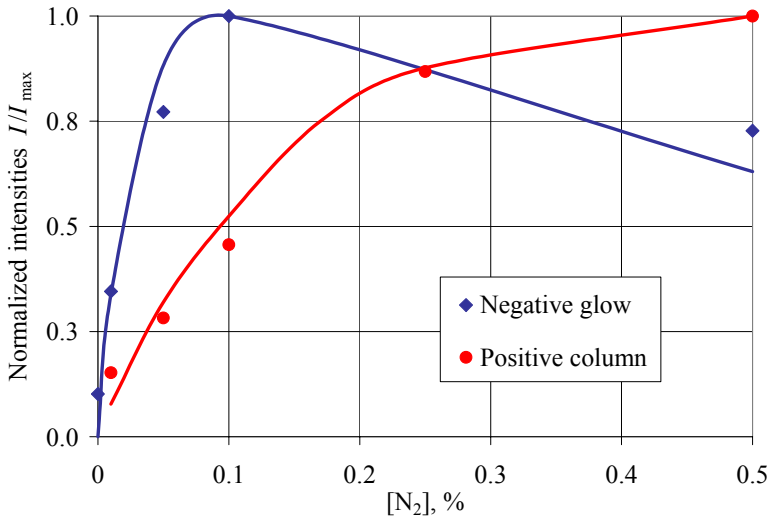

Figure 36. Normalized intensities of the N_2^+ (B-X) bandhead, λ = 391.4 nm, as a function of $[N_2]$ in negative glow and positive column regions; points- measurements at [e] $\approx 7 \cdot 10^{12}$ cm^{-3}, p = 60 Torr, axial direction, solid lines- calculated normalized densities, $[N_2^+(B)]$.

In the case of negative glow $[M^+]$=0. In the positive column the order of magnitude of $[M^+]$ was 10^{12} cm^{-3} and it was almost independent of $[N_2]$. Figure 37 shows calculated densities $[He_2^+]$ and $[N_2^+]$ as a function of $[N_2]$.

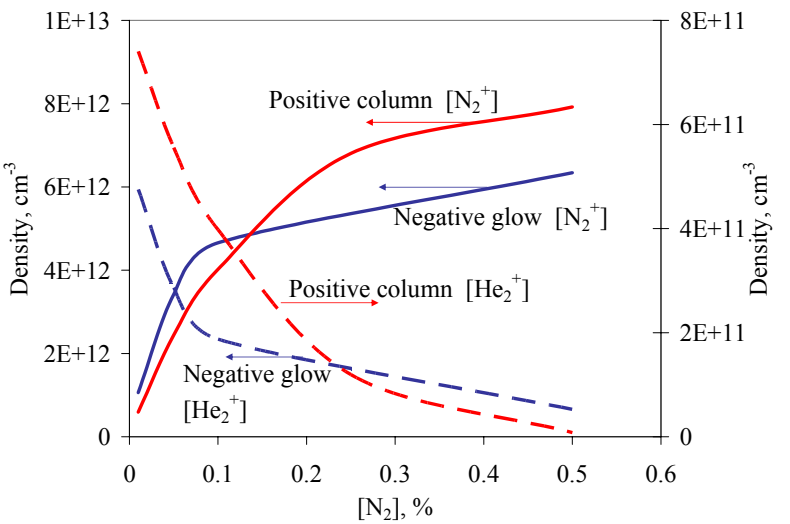

Figure 37. Calculated densities $[He_2^+]$ and $[N_2^+]$ as a function of $[N_2]$ for positive column and negative glow regions; [e] $\approx 7 \cdot 10^{12}$ cm^{-3}, p = 60 Torr.

The obtained density [He_2^+] and the experimentally determined density of [He(2^3S)] allows to estimate the relative importance of charge transfer and Penning reactions in N_2^+ production, figure 38. In the negative glow rates of these reactions were close to each other, the ratio of rates of reactions, $R_{Pe/CT}$ was in the range 0.3–0.6. At the same time in the positive column $R_{Pe/CT}$ increased with the growth of [N_2] from 5 to 160. The low importance of charge transfer reaction in the positive column is mainly caused by a small concentration of He_2^+.

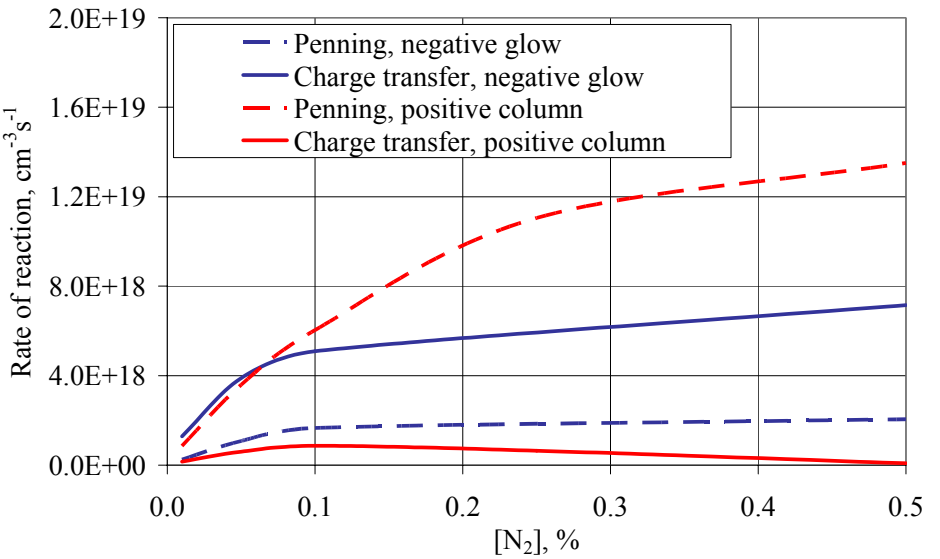

Figure 38. Rates of Penning and charge transfer reactions reaction in negative glow and positive column regions as a function of [N_2]. [e] $\approx 7\cdot10^{12}$ cm^{-3}, p = 60 Torr.

Besides, the known densities of [He_2^+] and [He(2^3S] allows to make some conclusions about the importance of different He_2^+ production mechanisms (figure 39). First, the associative ionization, reaction (1), is not important both in the negative glow and the positive column. The negligible importance of this reaction is mainly caused by a small concentration of excited atoms $He^*(n > 2)$. Atoms $He^*(n = 2)$ do not take part in the reaction (1) due to the insufficient translational energy.

Secondly, in the negative glow the He_2^+ production by reactions involving helium metastables, (2), (2'), (2'') is also unimportant. Indeed, in the negative glow density [He(2^3S)] is much smaller than that in positive column (figure 33), but [He_2^+] is almost an order of magnitude larger than that in positive column (figure 37). Hence in the negative glow He_2^+ should be mainly produced by He^+ conversion reaction (5). In the negative glow He^+ ions appear via He(1^1S) impact with fast electrons origin from high-field regions near the capillary walls, reaction (4). At the same time in the positive column where [He(2^3S)] is

much higher, He_2^+ ions could be produced both by reactions involving He metastables ((2), (2'), (2'')) and He^+ conversion, (5).

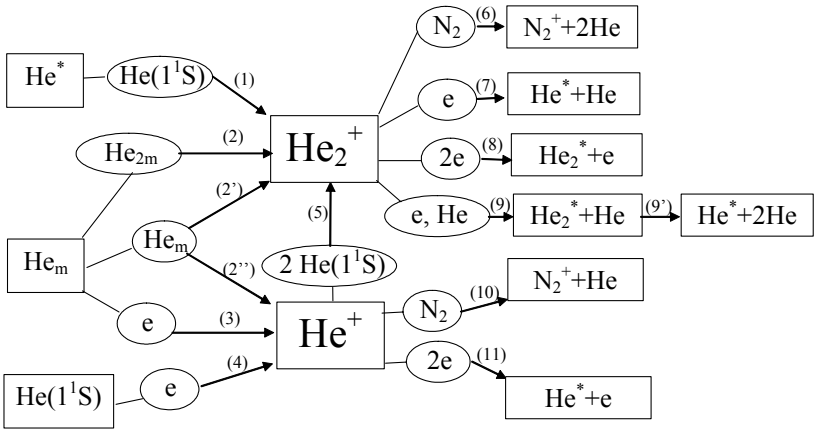

Figure 39. Schematic diagram of He ion production and loss mechanisms in He / N_2 mixture. Drawn on the basis of subsection 2.2.

4.4.4. Excitation of He states

Main excitation mechanisms of He states and selected radiative transitions are shown in figure 40. The diagram is drawn on the basis of data taken from [Weise, 1969] and [Huber, 1979].

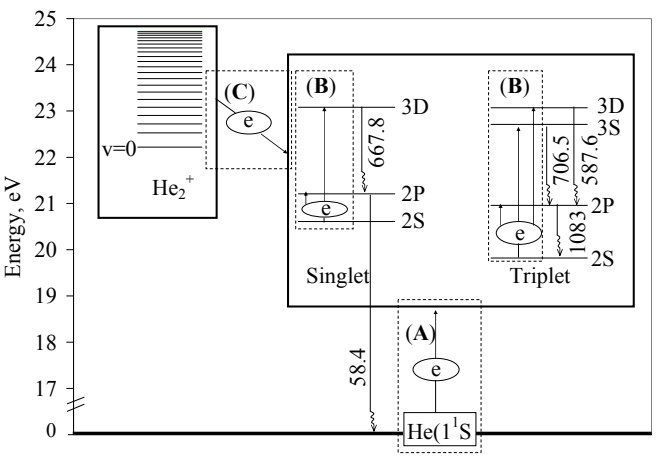

Figure 40. He excitation mechanisms and selected radiative transitions. Boxes with dashed borders represents different He excitation mechanisms: (A) – direct excitation, (B) – stepwise excitation from He metastable state atoms and (C) – excitation via He_2^+ dissociative recombination.

Excited states of He could be produced by the electron impact with ground state He(1^1S) atoms, box (A) in figure 40, by the stepwise excitation via metastable atoms, He(2^3S)and He(2^1S) (boxes B), and due to He_2^+ dissociation reactions (box C). In the following the relative importance of these mechanisms is discussed.

(A) excitation by electron impact with He(1^1S) (direct excitation).

The comparison of intensities of 667.8 nm (transition He(3^1D–2^1P)) and 587.6 nm (He(3^3D–2^3P)) lines gives a possibility to estimate the importance of this excitation path. The energies of the upper states of the corresponding transitions, $\varepsilon_s \approx 23.07$ eV, as well as the probabilities of radiative transitions, $A_{668} = 6.38 \cdot 10^7\ s^{-1}$ and $A_{587} = 7.06 \cdot 10^7\ s^{-1}$, of these lines are almost equal but as the spin conserving excitation is more favourable than the spin changing one, the excitation cross section of transition He(1^1S–3^1D) is higher than that of He(1^1S–3^3D) [John, 1964]. Thus, assuming the direct excitation, the intensity of the 667.8 nm line should be higher than the intensity of the 587.6 nm line.

Figures 35 and 41 demonstrates that in the positive column 587.6 nm line is more intensive and thus it is unlikely that the excitation occurs due to the direct excitation.

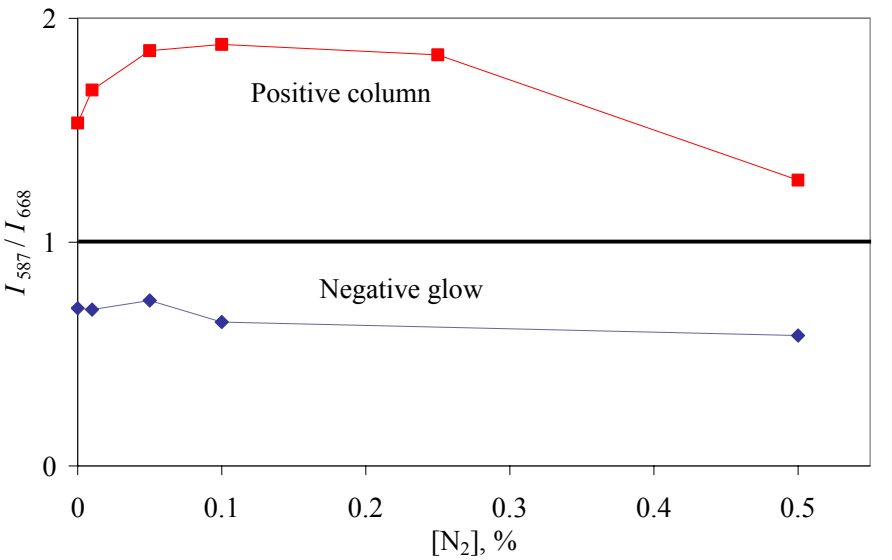

Figure 41. Ratio of measured intensities, I_{587}/I_{668}, as a function of N_2 fraction in the positive column and negative glow regions, [e] $\approx 7 \cdot 10^{12}$ cm^{-3}, p = 60 Torr, axial direction.

In the negative glow $I_{587}/I_{668} < 1$, therefore in this region one could expect the direct excitation of He states. In the negative glow the direct excitation of He occurs by the fast, non-equilibrium electrons. In [Arhipenko, 2005] it is shown

that in this case at the constant current density the intensity of lines which origin from He(n > 2) atoms, remains almost constant in the range [N_2]=0…1%. However, from figure 42 follows that in our case the intensities of lines starting from He(n > 2) states fall with the increase of [N_2] more than 50%.

Consequently, both in the negative glow and the positive column the direct excitation is not the dominant excitation mechanism.

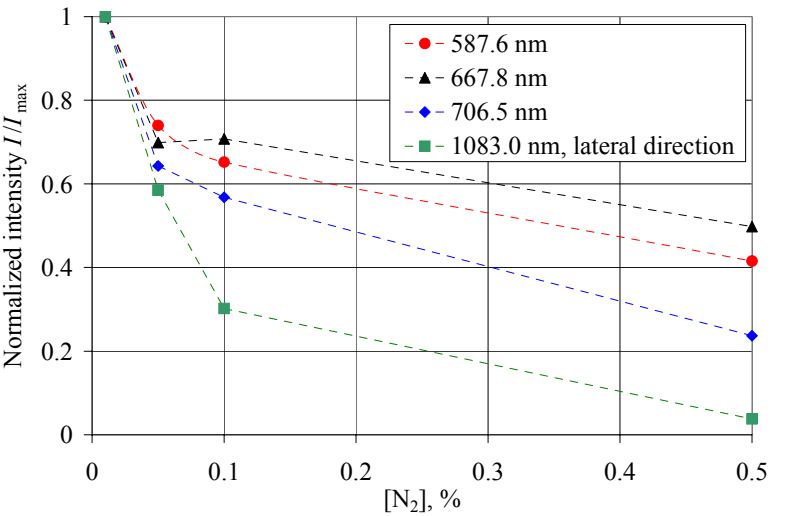

Figure 42. The intensities of He spectral lines as a function of [N_2]; negative glow region; [e] ≈ $7 \cdot 10^{12}$ cm^{-3}, p = 60 Torr; 1083.0 nm line was recorded in the lateral directions, other lines in the axial direction.

(B) Stepwise excitation via He metastable atoms.

The intensity ratio of 587.6 and 667.8 nm lines in figure 41 gives also a possibility to decide about the importance of stepwise excitation. It is known [Silfvast, 2004] that the interaction between singlet and triplet systems is weak, thus the stepwise excitation of singlet system states runs mostly via singlet metastable state, 2^1S and that of triplet states via triplet metastable, 2^3S, state. The excitation cross-sections by electron impact for transitions He(2^1S–3^1D) and He(2^3S–3^3D) are close in a wide range of electron energies [Beigman, 2000], therefore the intensities of the corresponding spectral lines are determined by the population of 2^1S and 2^3S states. The population of the He(2^3S) state is considerably higher than that of He(2^1S) as (i) the cross-section of transition He(1^1S–2^3S) is larger than He(1^1S–2^1S) [Pichou, 1976]; (ii) the He(2^1S) state is depopulated to the He(2^3S) state by electron impact [Mewe, 1970]; (iii) the 2^1S state is strongly coupled with the He(2^1P) state which has a short lifetime. Thus, if the stepwise excitation dominates, the intensity of the 587.6 nm line should exceed that of the 667.8 nm line. According to figure 41 in the positive column this condition is fulfilled.

(C) Population of He states via He_2^+ dissotiative recombination.

Previous analysis showed that in the negative glow neither direct nor stepwise excitation is the dominant excitation mechanisms of He states. Thus, in this region He states should be populated mainly via He_2^+ dissociative recombination. Comparing with the positive column, dissociative recombination is in the negative column more expected because:

(i) the concentration of He_2^+ is much higher.

(ii) in the negative glow the electron temperature of bulk electrons is very low and according to ([Carata, 1999], [Urbain, 2005]) the cross section of dissociative recombination of $He_2^+(v \geq 3)$ diminishes rapidly with the growth of electron temperature.

As it follows from subsection 2.2, the dissociative recombination runs either via two body reaction $He_2^+(v \geq 3) + e \rightarrow He_2^* \rightarrow He(n \geq 3) + He$ or three body reaction $He_2^+(v < 3) + e + He(e) \rightarrow He_2^* + He(e) \rightarrow He(n = 2) + He + He(e)$. Although He_2^+ forms always in a high vibrational state ($v \approx 15$) [Deloche, 1976], at our pressure the vibrational relaxation is fast (due to the reaction 2.18), i.e. concentration of $He_2^+(v < 3)$ is high and thus relative importance of three body recombination should be also high. According to [Pedersen, 2005], [Emmert, 1988] ca 60% of $He_2^+(v < 3)$ recombination produce $He(2^3P)$. Thus, if the dissociative recombination is the dominant mechanism of excitation He states, a correlation between $[He_2^+]$ and intensity of line 1083.0 nm (transition 2^3P-2^3S) should be expected. Figure 43 shows that in the negative glow the dependence of He 1083.0 nm line intensity on $[N_2]$ follows the dependence for $[He_2^+]$.

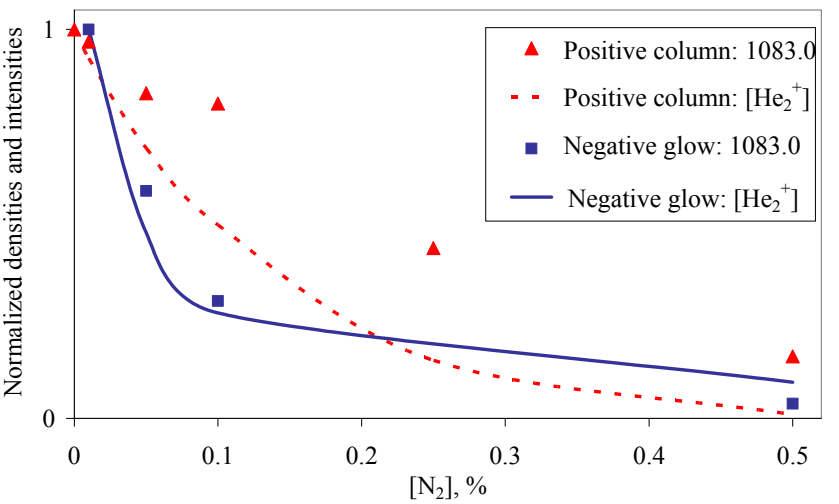

Figure 43. Normalized values of densities of $[He_2^+]$ (calculated, see subsection 4.4.3) and normalized intensity of the He line at λ = 1083.0 nm (lateral direction) as a function of $[N_2]$, $[e] \approx 7 \cdot 10^{12}$ cm^{-3}, p = 60 Torr. Points – experiment, line – calculation.

However, at low pressure afterglow studies [Ivanov, 1983], [Afanasjev, 1973], [Collins, 1969] it was found that the three body recombination is accompanied by He_2 radiation. In our spectra (figures 26 and 28), the radiation intensity at the wavelength ranges where He_2 bands should appear was weak, and the only band which could belong to He_2 was near 640 nm. The lack of He_2 bands in our spectra is explainable assuming He_2^* quenching by ground state He atoms and/or by impurities.

Our conclusion that in the negative glow the dissociative recombination is the dominating excitation mechanism of He states contradicts with the conclusion presented in [Kubota, 1991]. This study was carried out in conditions, which were close to ours. The authors of this paper stated that in the DC discharge the excitation of He states occurs due to dissociative recombination while in the HF stationary discharge dissociative recombination has a very low weight. This statement was based on the comparison of intensity distribution of DC and HF discharges along the discharge axis. Differently from DC discharge, in HF discharge the spatial distribution of the intensity was the same for all spectral lines. From this experimental finding the authors concluded that the excitation in HF discharge occurs by direct excitation. However, more likely the difference between the intensity distributions of DC and HF discharges reflects the circumstances that in the HF discharge the ions stay immovable during a cycle of oscillations and the excitation of He states occurs at places where He_2^+ ions are formed.

In summary, as it follows from preceding analysis, in the negative glow the excitation of He states occurs mainly via He_2^+ dissociative recombination while in the positive column stepwisely via He metastable state atoms.

4.5. Open problems

In the present study it was clarified the main N_2^+ production and He state excitation mechanisms in the negative glow and positive column regions. But there are open problems which demand further studies:

- First open problem concerns the lack of He_2 bands radiation which was expected in the spectra of the negative glow. The only band which could belong to the He_2 was near 640 nm (transition d–b, 0–0). According to literature data [Parker, 1981], besides the radiative transitions the transfer between He_2 states occurs also by He_2^* impact with He. This could be the reason why we did not saw in our spectra bands observed at lower pressures ([Ivanov, 1983], [Afanasjev, 1973]). Thus additional information about the excitation of He_2 should give the recording of spectra as a function of pressure.
- Second open problem concerns the excitation and quenching of N_2. Our preliminary analysis showed that in the case of negative glow, the intensity of N_2 bands correlates well with that of N_2^+ radiation. This could be

interpreted as cascade excitation of corresponding N_2 states from N_2^+. However, in the case of positive column a clear relationship between N_2^+ and N_2 intensities was missing and thus obviously other mechanisms like direct excitation from the N_2 ground state, stepwise excitation due electron impact with metastables N_2(a,A) etc, are responsible for N_2 excitation. For more precise answer about N_2 excitation and quenching mechanisms the concentration of N_2 metastable molecules should be determined.

SUMMARY

The aim of the present study was to find out the main excitation mechanisms of He atoms and ionization mechanisms of N_2 in He / N_2 mixtures of γ -mode HF discharge in negative glow and positive column regions. Experiments were carried out at middle pressures in He / N_2 mixtures with N_2 addition up to 0.5%. From electrical parameters *i-u* curves at different N_2 concentrations were recorded and phase shift between *i* and *u* was determined. On the basis of results of electrical measurements the electron density was calculated. Discharge spectra as a function of discharge current, total pressure and N_2 concentration were recorded. Experimental results allowed to calculate the rotational temperature of N_2^+(B) state and the concentration of He metastable atoms. The model based on the above-presented experimental data allowed to clarify the dominating excitation and ionization mechanisms.

The main results of the present study are:

- A method which allows to determine He excitation paths and N_2 ionization mechanisms in He / N_2 mixtures was developed. The method takes into account the more important plasma-chemical reactions and experimentally determined intensities of diagnostic spectral lines. It is assumed that the condition of quasineutrality is fulfilled. The method was applied for investigation of both, the negative glow and positive column regions.
- In the negative glow region He is excited dominantly via He_2^+ recombination in reactions $He_2^+ + e \rightarrow He^* + He$ and $He_2^+ + e + He \rightarrow He_2^* + He \rightarrow He^* + 2He$. Ions N_2^+ are produced mainly via charge transfer reaction, $He_2^+ + N_2 \rightarrow N_2^+ + 2He$. In the positive column region dominant He excitation mechanism is stepwise excitation, $He_m + e \rightarrow He^* + e$ while N_2 ionization occurs in Penning reaction, $He_m + N_2 \rightarrow N_2^+ + He + e$.
- Excitation of impurity gases (O, H) is in the positive column more efficient than that in the negative glow. At the same time the ionization rate of N_2 in the negative glow is higher.
- In the positive column even very small additions of N_2 have strong influence on the electron energy distribution function (EEDF).

SUMMARY IN ESTONIAN

Kõrgsagedusliku kapillaarlahenduse negatiivse helenduse ja positiivse samba uurimine

Heelium on põhikomponendiks paljudes seadmetes (UV-lambid, laserid), kus kasutatakse madalatemperatuurilist mittetasakaalulist plasmat. Tänu heeliumi suurele soojusjuhtivusele on võimalik tekitada ruumiliselt homogeenset plasmat suurtel lahendusse antavatel energiatel ka atmosfäärilähedastel rõhkudel. Samas on heeliumis tekitatud plasma karakteristikud tundlikud lisandite suhtes, sest tema metastabiilsete seisundite energia ületab enamiku teiste gaaside ionisatsioonienergiat. Seetõttu mõjutavad ka juba väga väikesed lisandi kontsentratsioonid ergastus- ja ionisatsiooniprotsesside dünaamikat.

Vaatamata väga suurele tööde hulgale, mis on seotud heeliumis tekitatud plasmaga, puudub uurijate seas siiani üksmeel erinevate plasmakeemiliste reaktsioonide osatähtsusest. Muuhulgas on väga vastandlikke tulemusi saadud uurimustes, mis puudutavad He_2^+ rekombinatsiooniahelat. Olulisi lahknevusi on ka reaktsioonide ahelas, mis viib lisandgaaside ioniseerimisele.

Käesoleva uurimistöö põhilisteks eesmärkideks oli

1. välja selgitada He ergastusmehhanismid ja
2. täpsustada N_2 molekulaarsete ioonide tekkemehhanismid lahenduse negatiivse helenduse ja positiivse samba piirkondades keskmistel rõhkudel.

Oma iseloomult oli töö eksperimentaalne, tulemuste interpeteerimisel seostati plasma spektraalkarakteristikud energeetiliste karakteristikutega.

Kõrgsagedusplasma (sagedus 27 MHz) tekitati kapillaaris He / N_2 segudes rõhkude vahemikus 20–200 Torr. Eksperimendiseade lubas eraldi uurida nii negatiivse helenduse kui ka positiivse samba piirkonda. Mõlemas lahenduse piirkonnas registreeriti intensiivsuse jaotus kapillaaris. Elektrilistest parameetritest mõõdeti volt-amper karakteristika ja faasivahe varieerides N_2 kontsentratsiooni. Elektrimõõtmiste alusel leiti elektronide kontsentratsioon. Spektrid registreeriti intervallis 300–1200 nm. Spektrite sõltuvus voolutugevust, N_2 kontsentratsioonist ja kogurõhust registreeriti nii piki kui ka risti kapillaari teljega. Spektraalmõõtmistulemuste põhjal leiti He metastabiilses seisundis olevate aatomite He(2^3S) kontsentratsioon, N_2^+ (B-X, 0-0) rotatsioonspektrit kasutades arvutati rotatsioontemperatuur. Ülaltoodud eksperimenditulemused lubasid leida plasmas asetleidvad domineerivad ergastus- ja ionisatsioonimehhanismid.

Käesoleva töö põhitulemused on järgmised:

- Töötati välja meetod, mis võimaldab määrata He ergastusmehhanismid ja N_2 ioonide tekkemehhanismid lahenduse negatiivse helenduse ja positiivse samba piirkondades He / N_2 segudes. Meetod baseerub He-N_2 plasmakeemiliste reaktsioonide analüüsil kombineerituna spektraalanalüüsiga ja eeldusel, et eelpool nimetatud lahenduspiirkonnad on tervikuna elektriliselt

neutraalsed. Meetodi eeliseks on rakendatavus ka juhul, kui puudub tasakaal elektrivälja tugevuse ja elektronide energiaspektri vahel.

- Negatiivses helenduses domineerib He ergastamine He_2^+ rekombinatsiooni-reaktsioonides, $He_2^+ + e \rightarrow He^* + He$ ja $He_2^+ + e + He \rightarrow He_2^* + He \rightarrow He^* + 2He$. Ioonid N_2^+ tekitatakse valdavalt laenguvahetusreaktsioonis, $He_2^+ + N_2 \rightarrow N_2^+ + 2He$.

  Positiivses sambas toimub He ergastamine elektronpõrkega He metastabiilses seisundis oleva aatomiga, $He_m + e \rightarrow He^* + e$, ioonid N_2^+ tekivad Penningi reaktsiooni tulemusena, $He_m + N_2 \rightarrow N_2^+ + He + e$.
- Jääkgaaside (O, H) ergastamine positiivses sambas on oluliselt efektiivsem võrreldes negatiivse helendusega. Samas N_2^+ teke on tunduvalt intensiivsem negatiivses helenduses.
- Positiivses sambas muudavad juba väga väikesed N_2 kontsentratsioonid heeliumis elektronide energia jaotusfunktsiooni.

ACKNOWLEDGEMENTS

First of all I am very thankful to Assoc. Prof. Matti Laan for supervision and for his continuous support.

I wish to thank Dr. Märt Aints for interesting discussions concerning discharge equivalent schema.

I would like to thank Mr. Tõnu Asu for the solution of several difficult technical problems.

I would like to thank all colleagues in the Gas Discharge Laboratory of the Tartu University for their useful advices.

Finally, my greatest thanks to my family for their permanent support.

REFERENCES

1. Afanasjev N V, Gerassimov G N and Stardseva G P 1973 *Optics and spectroscopy* **34** 664–7. In Russian.
2. Alves L L and Ferreira C M 1991 *J. Phys. D* **24** 581–92
3. Alves L L, Gousset G and Ferreira C M 1992 *J. Phys. D* **25** 1713–32
4. Arkhipenko V I, Kirillov A A, Simonchik LV and Zgirouski S M 2005 *Plasma Sources Sci. Technol.* **14** 757–65
5. Ashurbekov N A, Kurbanismailov V S, Omarov O A and Omarova N O 2000 *High Temperature* **38** 795–810
6. Bates D R 1979 *J. Phys. B: At. Mol. Phys.* **12** L35–8
7. Beigman I L, Vainshtein L A, Brix M, Pospieszczyk A, Bray I, Fursa D V and Ralchenko Yu V 2000 *At. Data Nucl. Data Tables* **74** 123–53
8. Belikov A E 1997 *J. Chem. Phys.* **215** 97–109
9. Berrington K A and Kingston A E 1987 *J. Phys. B: At. Mol. Phys.* **20** 6631–40
10. Bibinov N k, Fateev A A and Weismann K 2001 *Plasma Sources Sci. Tehnol.* **10** 579–88
11. Boeuf J P 2003 *J. Phys. D: Appl. Phys*. **36** R53-R79
12. Born G K 1968 *Phys. Rev.* **169** 155–64
13. Böhringer H,Glebe W and Arnold F 1983 *J. Phys. B: At. Mol. Phys.* **16** 2619–26
14. Brongersma H, Knoop F W and Back C 1972 *Chem. Phys. Lett.* **13** 16–9
15. Carata L and Orel A E 1999 *Phys. Rev. A* **59** 2804–12
16. Chutjian A and Thomas L D 1975 *Phys. Rev. A* **11** 1583–95
17. Collins C B and Hurt W B 1969 *Phys. Rev*. **179** 203–97
18. DeJoseph C A, Demidov V I, Blessington J and Koepke M E 2007 *J. Phys. B: At.Mol. Opt. Phys* **40** 3823–33
19. Deloche R, Monchicourt P, Cheret M and Lambert F 1976 *Phys. Rev. A* **13** 1140–76
20. Demidov V, Rudakova T, Rytenkov S and Skrebov V 1991 *J. Phys. B: At.Mol. Opt. Phys* **24** 4281–91
21. Dothan F and Kagan Yu M 1981 *J. Phys. D* **14** 183–97
22. Dunkin D B, Fehsenfeld F C, Schmeltekopf A L and Ferguson E E 1968 *J. Chem. Phys*. **49** 1365–71
23. Emmert F, Angermann H H, Dux R and Langhoff H 1988 *J. Phys. D* **21** 667–74
24. Endoh M, Tsuji M and Nishimura Y 1983 *J. Chem. Phys*. **79** 5368–75
25. Farragher A L 1970 *Trans. Faraday Soc.***66** 1411–22
26. Fehsenfeld F C, Schmeltekopf A L, Goldan P D, Schiff H I and Ferguson E E 1966 *J. Chem. Phys*. **44** 4087–94
27. Frish S E 1970 Spectroscopy of a Gas-Discharge Plasma(Leningrad: Nauka)
28. Frost M J and Sharpe C R J 2001 *Phys. Chem. Chem. Phys.* **3** 4536–41
29. Garrison B J, Miller W H and Schaefer H F 1973 *J. Chem. Phys.* **59** 3193–98
30. Gordiets B F, Ferreira C M, Guerra V L, Loureiro J M A H, Nahorny J, Pagnon D, TouZeau M and Vialle 1995 *IEEE Trans. Plasma Sci*. **26** 750–68
31. Hasilev V J, Mihalevskii V S and Tolmatsev G N 1980 *Plasma Physics* **6** 430–5. In Russian.
32. Hill P C and Herman P R 1993 *Phys. Rev. A* **47** 4837–44
33. Hinnov E and Hirschberg J G 1962 *Phys. Rev.* **125** 795–801
34. Hotop H and Niehaus A 1970 *Intern. J. Mass Spectrom. Ion Phys.* **5** 415–41
35. Huber K P and Herzberg G 1979 *Molecular spectra and Molecular Structure: IV. Constants of Diatomic Molecules* (New York: Van Nostrand)

36. Ivanov V A and Skoblo Yu E 1988 *Opt. Spectrosc.* **65** 750–753. In Russian.
37. Ivanov V A, Penkin N P and Skoblo Yu E 1983 *Opt. Spectrosc.* **54** 927–9. In Russian.
38. Jitsuno T 1981 *J. Phys. D: Appl. Phys.* **14** 1377–84
39. John R M St, Miller F L and Lin C C 1964 *Phys. Rev. A* **4** A888–97
40. Johnson A W and Gerardo J B 1973 . *Phys. Rev. A* **7** 925–8
41. Kubota T, Morisaki Y, Ohsawa A and Ohuchi M 1992 *J. Phys. D: Appl. Phys.* **25** 613–9
42. Kutasi K, Hartmann P and Donko Z 2001 *J. Phys. D: Appl. Phys.* **34** 3368–77
43. Lagus M E, Boffard J B, Anderson and Lin C C 1996 *Phys. Rev. A* **53** 1505–18
44. Laux C O and Kruger C H 1992 Arrays of radiative transition probabilities for the N_2 first and second positive, NO beta and gamma, N^+_2 first negative, and O_2 Schumann—Rungeband systems *J. Quant. Spectrosc. Radiat. Transfer* **48** 9–14
45. Lawler J E, Den Hartog E A and Hitchon W N G 1991 *Phys. Rev. A* **43** 4427–37
46. Lee F W Collins C B and Waller R A 1976 *J. Chem. Phys.* 65 1605-
47. Levaton J, Amorim J, Souza A R, Franco and Ricard A 2002 *J. Phys. D: Appl. Phys.* **35** 689–99
48. Leventhal J J, Earl J D and Harris H H 1975 *Phys. Rev. Lett.* **35** 719–22
49. Lide D R (ed) 1997 *CRC Handbook of Chemistry and Physics* 77th edn (Boca Raton, FL: CRC Press).
50. Mewe R 1970 *Physica* **47** 373–97
51. Märk T and Oskam H J 1971 *Phys. Rev. A* **4** 1445–52
52. Myers H 1963 *Phys. Rev* **130** 1639–43
53. Naghizadeh-Kashani Y, Cressault Y and Gleizes A 2002 *J. Phys. D: Appl. Phys.* **35** 2925–34
54. Obernoi R S and Nesbet R K 1973 *Phys. Rev. A* **8** 2969–79
55. Paris P, Aints M, Laan M, Valk F 2004 *J. Phys. D: Appl. Phys.* **37** 1179–84
56. Parker J W, Anderson L W, Fitzsimmons W A and Lin C C 1981 *J. Chem. Phys.* **75** 1804–9
57. Pavlovskaja E H and Podmochenskii I V 1973 *Opt. Spectrosc.* **34** 19–24 (in Russian).
58. Pedersen H B, Buhr H, Altevogt S, Andrianarijaona V, Kreckel H, Lammich L, de Ruette N, Staicu-Casagrande E M, Schvalm D, Strasser D, Urbain X, Zajfman D and Wolf A 2005 *Journal of Physics: Conference Series* **4** 168–76
59. Petrov G M, Matte J P, Peres I, Margot J, Sadi T, Hubert J, Tran K C, Alves L L, Loureiro J, Ferreira C M, Guerra V and Gousset G 2000 *Plasma Chemistry and Plasma Proccessing* **20** 183–207
60. Phelps A V 1955 *Phys. Rev.* **99** 1307–13
61. Pichou F, Huetz A Joyez G Landau M and Mazeau J 1976 *J. Phys. B: At. Mol Phys.* **9** 933–44
62. Piech G A, Lagus M E, Anderson L W and Lin C C 1997 *Phys. Rev. A* **55** 2842–56
63. Pouvesle J M and Bouchoule 1982 *J. Chem. Phys.* **77** 817–25
64. Raizer Y P 1991 Gas Discharge Physics (Berlin: Springer)
65. Raizer Y P and Yatsenko N A 1996 Radio-frequency capacitive discharges and gas lasers with RF excitation Gas Lasers-Recent Developments and Future Prospects ed W I Witteman and V N Ochkin (Dordrecht: Kluwer) pp 37–54
66. Ralchenko, Yu, Kramida, A E, Reader, J, and NIST ASD Team 2008 NIST Atomic Spectra Database (version 3.1.5), [Online]. Available:

http://physics.nist.gov/asd3 [2009, January 12]. National Institute of Standards and Technology, Gaithersburg, MD.
67. Reich N 1994 Transversale kapazitive Hochfrequenzanregung von Gasentladungs-lasern *PhD Thesis* Ruhr-Univerität Bochum pp 19–21
68. Rogers W A and Biondi M A 1964 *Phys. Rev* **134** A1215–24
69. Roos O 1959 *J. Chem. Phys.* **30** 729–34
70. Schmeltekopf A L, Ferguson E E and Fehsenfeld F C 1968 *J. Chem. Phys.* **48** 2966–73
71. Schmeltekopf A L and Fehsenfeld F C 1970 *J. Chem. Phys.* **53** 3173–7
72. Silfvast W T 2004 Laser fundamentals (Cambridge University Press)
73. Slovetskii D I 1980 Mechanisms of Chemical Reactions in Non-Equilibrium Plasmas (Moscow: Nauka)
74. Smirnov B M 1974 Ions and Excited Atoms in Plasma (Moscow: Atomizdat) (in Russian)
75. Soldatov A N and Sorokin G M 1976 *Izv. VUZ Fiz.* **6** 136–8
76. Urbain X, Djuric N, Safvan C P, Jensen M J, Pedersen H B, Sogaard L Vejby and Andersen L H 2005 *J. Phys. B: At.Mol. Opt. Phys* **38** 43–50
77. Warneck P 1967 *J. Chem. Phys.* **47** 4279–81
78. Weise W L, Smith M W and Miles B M 1969 *Atomic Transition Probabilities (US National Bureau of Standards Reference Data Series 22)* vol 22 (Washington, DC: USGPO)
79. Yang X, Moravej M, Nowling G R, Babayan S E, Panelon J, Chang J P and Hicks R F 2004 Plasma Sources Sci. Technol. 14 314–20

PUBLICATIONS

CURRICULUM VITAE

Jüri Raud

General data

Date and place of birth: 06.08.1972, Kohila, Estonia
Citizenship: Estonia
Address: University of Tartu, Institute of Physics,
Tähe 4, 51010, Tartu, Estonia
GSM: +(372) 5391 1632
E-mail: jyri.raud@ut.ee

Education

1980–1983	Vana-Vigala Elementary School
1983–1987	Kivi-Vigala Primary School
1987–1990	Pärnu-Jaagupi Secondary School
1990–1995	University of Tartu, BSc (geology)
1995–1999	University of Tartu, BSc (physics)
1999–2001	University of Tartu, MSc (physics)
2001–2006	University of Tartu, PhD student (physics)

Professional employment

1993–1994	RAS REI; computer programmer
2000–2007	University of Tartu, Institute of Experimental Physics and Technology; senior engineer
2007–present	Institute of Physics, extraordinary researcher

ELULOOKIRJELDUS

Jüri Raud

Üldandmed

Sünniaeg ja -koht:	06.08.1972, Kohila, Eesti
Kodakondsus:	Eesti
Aadress:	Tartu Ülikool, Füüsika Instituut, Tähe 4, 51010, Tartu
GSM:	+(372) 5391 1632
E-mail:	jyri.raud@ut.ee

Hariduskäik

1980–1983	Vana-Vigala Algkool
1983–1987	Kivi-Vigala Põhikool
1987–1990	Pärnu-Jaagupi Keskkool
1990–1995	Tartu Ülikool, BSc (geoloogia)
1995–1999	Tartu Ülikool, BSc (füüsika)
1999–2001	Tartu Ülikool, MSc (füüsika)
2001–2006	Tartu Ülikool, doktorantuur (füüsika)

Teenistuskäik

1993–1994	RAS REI; programmeerija
2000–2007	Tartu Ülikool, Eksperimentaalfüüsika ja Tehnoloogia Instituut, vaneminsener
2007–tänaseni	Tartu Ülikool, Füüsika Instituut, erakorraline teadur.

DISSERTATIONES PHYSICAE UNIVERSITATIS TARTUENSIS

1. **Andrus Ausmees.** XUV-induced electron emission and electron-phonon interaction in alkali halides. Tartu, 1991.
2. **Heiki Sõnajalg.** Shaping and recalling of light pulses by optical elements based on spectral hole burning. Tartu, 1991.
3. **Sergei Savihhin.** Ultrafast dynamics of F-centers and bound excitons from picosecond spectroscopy data. Tartu, 1991.
4. **Ergo Nõmmiste.** Leelishalogeniidide röntgenelektronemissioon kiiritamisel footonitega energiaga 70–140 eV. Tartu, 1991.
5. **Margus Rätsep.** Spectral gratings and their relaxation in some low-temperature impurity-doped glasses and chrystals. Tartu, 1991.
6. **Tõnu Pullerits.** Primary energy transfer in photosynthesis. Model calculations. Tartu, 1991.
7. **Olev Saks.** Attoampri diapasoonis voolude mõõtmise füüsikalised alused. Tartu, 1991.
8. **Andres Virro.** AlGaAsSb/GaSb heterostructure injection lasers. Tartu, 1991.
9. **Hans Korge.** Investigation of negative point discharge in pure nitrogen at atmospheric pressure. Tartu, 1992.
10. **Jüri Maksimov.** Nonlinear generation of laser VUV radiation for high-resolution spectroscopy. Tartu, 1992.
11. **Mark Aizengendler.** Photostimulated transformation of aggregate defects and spectral hole burning in a neutron-irradiated sapphire. Tartu, 1992.
12. **Hele Siimon.** Atomic layer molecular beam epitaxy of A^2B^6 compounds described on the basis of kinetic equations model. Tartu, 1992.
13. **Tõnu Reinot.** The kinetics of polariton luminescence, energy transfer and relaxation in anthracene. Tartu, 1992.
14. **Toomas Rõõm.** Paramagnetic H^{2-} and F^+ centers in CaO crystals: spectra, relaxation and recombination luminescence. Tallinn, 1993.
15. **Erko Jalviste.** Laser spectroscopy of some jet-cooled organic molecules. Tartu, 1993.
16. **Alvo Aabloo.** Studies of crystalline celluloses using potential energy calculations. Tartu, 1994.
17. **Peeter Paris.** Initiation of corona pulses. Tartu, 1994.
18. **Павел Рубин.** Локальные дефектные состояния в CuO_2 плоскостях высокотемпературных сверхпроводников. Тарту, 1994.
19. **Olavi Ollikainen.** Applications of persistent spectral hole burning in ultrafast optical neural networks, time-resolved spectroscopy and holographic interferometry. Tartu, 1996.
20. **Ülo Mets.** Methodological aspects of fluorescence correlation spectroscopy. Tartu, 1996.
21. **Mikhail Danilkin.** Interaction of intrinsic and impurity defects in CaS:Eu luminophors. Tartu, 1997.

22. **Ирина Кудрявцева.** Создание и стабилизация дефектов в кристаллах KBr, KCl, RbCl при облучении ВУФ-радиацией. Тарту, 1997.
23. **Andres Osvet.** Photochromic properties of radiation-induced defects in diamond. Tartu, 1998.
24. **Jüri Örd.** Classical and quantum aspects of geodesic multiplication. Tartu, 1998.
25. **Priit Sarv.** High resolution solid-state NMR studies of zeolites. Tartu, 1998.
26. **Сергей Долгов.** Электронные возбуждения и дефектообразование в некоторых оксидах металлов. Тарту, 1998.
27. **Kaupo Kukli.** Atomic layer deposition of artificially structured dielectric materials. Tartu, 1999.
28. **Ivo Heinmaa.** Nuclear resonance studies of local structure in $RBa_2Cu_3O_{6+x}$ compounds. Tartu, 1999.
29. **Aleksander Shelkan.** Hole states in CuO_2 planes of high temperature superconducting materials. Tartu, 1999.
30. **Dmitri Nevedrov.** Nonlinear effects in quantum lattices. Tartu, 1999.
31. **Rein Ruus.** Collapse of 3d (4f) orbitals in 2p (3d) excited configurations and its effect on the x-ray and electron spectra. Tartu, 1999.
32. **Valter Zazubovich.** Local relaxation in incommensurate and glassy solids studied by Spectral Hole Burning. Tartu, 1999.
33. **Indrek Reimand.** Picosecond dynamics of optical excitations in GaAs and other excitonic systems. Tartu, 2000.
34. **Vladimir Babin.** Spectroscopy of exciton states in some halide macro- and nanocrystals. Tartu, 2001.
35. **Toomas Plank.** Positive corona at combined DC and AC voltage. Tartu, 2001.
36. **Kristjan Leiger.** Pressure-induced effects in inhomogeneous spectra of doped solids. Tartu, 2002.
37. **Helle Kaasik.** Nonperturbative theory of multiphonon vibrational relaxation and nonradiative transitions. Tartu, 2002.
38. **Tõnu Laas.** Propagation of waves in curved spacetimes. Tartu, 2002.
39. **Rünno Lõhmus.** Application of novel hybrid methods in SPM studies of nanostructural materials. Tartu, 2002.
40. **Kaido Reivelt.** Optical implementation of propagation-invariant pulsed free-space wave fields. Tartu, 2003.
41. **Heiki Kasemägi.** The effect of nanoparticle additives on lithium-ion mobility in a polymer electrolyte. Tartu, 2003.
42. **Villu Repän.** Low current mode of negative corona. Tartu, 2004.
43. **Алексей Котлов.** Оксианионные диэлектрические кристаллы: зонная структура и электронные возбуждения. Tartu, 2004.
44. **Jaak Talts.** Continuous non-invasive blood pressure measurement: comparative and methodological studies of the differential servo-oscillometric method. Tartu, 2004.
45. **Margus Saal.** Studies of pre-big bang and braneworld cosmology. Tartu, 2004.

46. **Eduard Gerškevitš.** Dose to bone marrow and leukaemia risk in external beam radiotherapy of prostate cancer. Tartu, 2005.
47. **Sergey Shchemelyov.** Sum-frequency generation and multiphoton ionization in xenon under excitation by conical laser beams. Tartu, 2006.
48. **Valter Kiisk.** Optical investigation of metal-oxide thin films. Tartu, 2006.
49. **Jaan Aarik.** Atomic layer deposition of titanium, zirconium and hafnium dioxides: growth mechanisms and properties of thin films. Tartu, 2007.
50. **Astrid Rekker.** Colored-noise-controlled anomalous transport and phase transitions in complex systems. Tartu, 2007.
51. **Andres Punning.** Electromechanical characterization of ionic polymer-metal composite sensing actuators. Tartu, 2007.
52. **Indrek Jõgi.** Conduction mechanisms in thin atomic layer deposited films containing TiO_2. Tartu, 2007.
53. **Aleksei Krasnikov.** Luminescence and defects creation processes in lead tungstate crystals. Tartu, 2007.
54. **Küllike Rägo.** Superconducting properties of MgB_2 in a scenario with intra- and interband pairing channels. Tartu, 2008.
55. **Els Heinsalu.** Normal and anomalously slow diffusion under external fields. Tartu, 2008.
56. **Kuno Kooser.** Soft x-ray induced radiative and nonradiative core-hole decay processes in thin films and solids. Tartu, 2008.
57. **Vadim Boltrushko.** Theory of vibronic transitions with strong nonlinear vibronic interaction in solids. Tartu, 2008.
58. **Andi Hektor.** Neutrino Physics beyond the Standard Model. Tartu, 2008.
59. **Raavo Josepson.** Photoinduced field-assisted electron emission into gases. Tartu, 2008.
60. **Martti Pärs.** Study of spontaneous and photoinduced processes in molecular solids using high-resolution optical spectroscopy. Tartu, 2008.
61. **Kristjan Kannike.** Implications of neutrino masses. Tartu, 2008.
62. **Vigen Issahhanjan.** Hole and interstitial centres in radiation-resistant MgO single crystals. Tartu, 2008.
63. **Veera Krasnenko.** Computational modeling of fluorescent proteins. Tartu, 2008.
64. **Mait Müntel.** Detection of doubly charged higgs boson in the CMS detector. Tartu, 2008.
65. **Kalle Kepler.** Optimisation of patient doses and image quality in diagnostic radiology. Tartu, 2009.